MARK2/MARK3 kinases are catalytic co-dependencies of YAP/TAZ in human cancer

Olaf Klingbeil[1], Damianos Skopelitis[1], Claudia Tonelli[1], Toyoki Yoshimoto[1], Aktan Alpsoy[1], Maria C. Panepinto[1], Francesca Minicozzi[1], Joseph R. Merrill[1], Amanda M. Cafiero[1], Disha Aggarwal[1,2], Suzanne Russo[1], Taehoon Ha[1], Osama E. Demerdash[1], Tse-Luen Wee[1], David L. Spector[1,2], Scott K. Lyons[1], David A. Tuveson[1], Paolo Cifani[1], and Christopher R. Vakoc[1,3*]

Affiliations:

[1]Cold Spring Harbor Laboratory, Cold Spring Harbor, New York, 11724, U.S.A.

[2]Graduate Program in Genetics, Stony Brook University, Stony Brook, New York 11794

[3]Lead contact

*Correspondence:

Christopher R. Vakoc

1 Bungtown Road

Cold Spring Harbor, New York 11724

United States

vakoc@cshl.edu

(1-516-367-5030)

Running title: MARK2/3 and YAP/TAZ are linked cancer dependencies

Competing interests

C.R.V. has received consulting fees from Flare Therapeutics, Roivant Sciences and C4 Therapeutics; has served on the advisory boards of KSQ Therapeutics, Syros Pharmaceuticals and Treeline Biosciences; has received research funding from Boehringer-Ingelheim and Treeline Biosciences; and owns a stock option from Treeline Biosciences. D.A.T. is a member of the Scientific Advisory Board and receives stock options from Leap Therapeutics, Surface Oncology, and Cygnal Therapeutics and Mestag Therapeutics outside the submitted work. D.A.T. is the scientific co-founder of Mestag Therapeutics. D.A.T. has received research grant support from Fibrogen, Mestag, and ONO Therapeutics. D.L.S. is a member of the Scientific Advisory Board of Flamingo Therapeutics and Amaroq Therapeutics. None of this work is related to the publication.

Abstract

The Hippo signaling pathway is commonly dysregulated in human cancer, which leads to a powerful tumor dependency on the YAP/TAZ transcriptional coactivators. Here, we used paralog co-targeting CRISPR screens to identify the kinases MARK2/3 as absolute catalytic requirements for YAP/TAZ function in diverse carcinoma and sarcoma contexts. Underlying this observation is direct MARK2/3-dependent phosphorylation of NF2 and YAP/TAZ, which effectively reverses the tumor suppressive activity of the Hippo module kinases LATS1/2. To simulate targeting of MARK2/3, we adapted the CagA protein from *H. pylori* as a catalytic inhibitor of MARK2/3, which we show can regress established tumors *in vivo*. Together, these findings reveal MARK2/3 as powerful co-dependencies of YAP/TAZ in human cancer; targets that may allow for pharmacology that restores Hippo pathway-mediated tumor suppression.

Significance:

We show how genetic redundancy conceals tight functional relationships between signaling and transcriptional activation in cancer. Blocking the function of MARK2/3 kinases leads to the reactivation of the Hippo tumor suppressive pathway and may have therapeutic potential in YAP/TAZ dysregulated carcinomas and sarcomas.

Introduction

The Hippo signaling pathway is a conserved regulator of cell identity and proliferation during metazoan development, with additional roles in tissue regeneration and in cancer progression (1). In mammals, the core of the Hippo pathway includes the kinases LATS1/2, which catalyze inhibitory phosphorylation of the YAP/TAZ transcriptional coactivators (2,3). LATS1/2 activity is, in turn, activated by MST1/2 and MAP4K kinases and by the scaffolding protein NF2, which are themselves regulated by signals from the tissue microenvironment (4-10). Once released from LATS1/2-mediated inhibition, YAP/TAZ can enter the nucleus and bind to TEAD transcription factors to activate a transcriptional program of cell proliferation and lineage plasticity (11-13).

YAP/TAZ and its upstream Hippo pathway are commonly dysregulated in human carcinomas and sarcomas to promote tumor development (14,15). This can occur via genetic (e.g. *YAP/TAZ* amplifications) (14) or non-genetic (e.g. perturbations of the extracellular matrix, metabolism, or cell polarity) (16-20) mechanisms, with a consequence being that many human cancers possess a powerful dependency on the function of YAP/TAZ to sustain tumor growth. Since YAP/TAZ activity is dispensable for the homeostasis of several tissues (21-23), the aberrant functioning of this pathway has motivated efforts to develop drugs that interfere with YAP/TAZ function, such as small molecules that block the interaction between YAP/TAZ and TEAD proteins (24-27). However, a major obstacle in this effort has been in identifying ‘druggable’ targets that allow for the restoration of Hippo-mediated tumor suppression in YAP/TAZ-dependent cancers.

MARK kinases (also known as PAR-1) are conserved regulators of cellular polarity and microtubule dynamics. Genetic screens performed in *C. elegans* first implicated Par1 as essential for asymmetric

cell divisions during early embryonic development through regulation of the mitotic spindle (28). Studies in several mammalian systems implicate MARK kinases (MARK1-4) as regulators of cell polarity through the phosphorylation of microtubule-associated proteins (29-31). In addition, evidence exists that MARK kinases regulate the output of other signaling pathways linked to cell proliferation, such as AMPK (32), Hippo (33), and MAPK (34). However, it is unclear from single gene knockout studies whether any of the human MARK kinases perform vital functions that support cancer growth, an issue that might be confounded by the genetic redundancy among the four MARK kinases.

Here we developed a CRISPR screening strategy to identify redundant paralog dependencies in cancer cell line models. Using this approach, we identified the kinase MARK2/3 as essential for the growth of cancer cell line models harboring YAP/TAZ activation. Using genetic, transcriptomic, and biochemical assays, we show that MARK2/3 supports YAP/TAZ function in cancer by inhibiting the Hippo signaling pathway. We define multiple substrates of MARK2/3 catalytic activity that account for its role in this pathway. Finally, we employed an inducible peptide-based inhibitor of MARK2/3 to demonstrate the anti-cancer activity of targeting these kinases *in vivo*. Collectively, this work reveals MARK2/3 as a druggable target that allows for upstream control of the YAP/TAZ oncoproteins in human cancer.

Results

Paralog co-targeting CRISPR screens identify MARK2/3 as context-specific cancer dependencies

Here, we developed a dual sgRNA CRISPR vector system for performing double knockout screens of gene paralogs in search of redundant cancer cell dependencies (**Fig. 1A**). Using this system, we cloned a pooled library of 64,697 dual guide RNAs designed to generate 1,719 single gene knockouts and 2,529 paralog double knockouts, focusing on genes involved in signal transduction and epigenetic regulation (**Fig. 1A**, **Supplementary Table 1,2**). For each gene, we designed sgRNAs targeting exons that encode conserved protein domains to maximize the efficiency of generating loss-of-function alleles (35). While prior studies have described CRISPR screening strategies for revealing epistatic gene interactions (36-42), we sought to apply our method to a larger cancer cell line panel to uncover context-specific dependencies that might have been overlooked previously. To this end, we performed negative-selection screens in 22 cancer cell lines grown under standard 2D culture conditions, representing a diverse set of tumor lineages and genotypes (**Supplementary Table 3**). The performance of control sgRNAs within this library supported the accuracy of these screening datasets (**Supplementary Fig. S1A-C**). For each double knockout, we quantified the degree of genetic redundancy using the GEMINI algorithm (43), which validated paralogs that are known to support cancer growth in a redundant manner, such as *HDAC1/HDAC2*, *ESCO1/ESCO2*, and *EP300/CREBBP* (**Fig. 1B**, **Supplementary Table 4-6**) (44-46). By excluding pan-essential paralog pairs required for all cancer cell lines tested, we nominated the kinase paralogs *MARK2* and *MARK3* as outliers showing robust redundancy and cell line selectivity as cancer dependencies (**Fig. 1B, Supplementary Fig. S1B, S1D**). While prior studies have identified functions for specific MARK kinases in cancer (47-49), the essential redundant function of MARK2/3 in human cancer cells has, to our knowledge, not been previously defined.

To validate these screening results, we performed arrayed format competition-based proliferation experiments in a panel of 31 cancer cell lines (**Fig. 1C**, **1D**, **Supplementary Fig. S1E, Supplementary Table 3**). These assays validated the redundancy and essentiality of MARK2/3 in 19 cancer lines, whereas 12 cancer lines proliferated normally despite effective MARK2/3 double knockout, confirmed by western blotting (**Fig. 1E, Supplementary Fig. S1F**). In these experiments, we noticed that MARK2/3 dependency was biased towards carcinomas and sarcomas, whereas most hematopoietic and neuroendocrine lineage cancers proliferated independently of MARK2/3 (**Fig. 1C**). Knockout of MARK2/3 led to a G0/G1 cell cycle arrest and apoptosis in pancreatic (YAPC) and breast (MDA-MB231) cancer lines, with a potency that resembled the effects of inactivating the mutant *KRAS* oncogene present in these models (**Fig. 1F, 1G, Supplementary Fig. S1G-I**). MARK2/3 knockout in YAPC xenografts led to robust tumor growth inhibition *in vivo* (**Supplementary Fig. S2A, S2B**). Expression of a CRISPR-resistant *MARK2* or *MARK3* cDNA alleviated the cell fitness defect caused by the double knockout, indicating on-target effects (**Fig. 1H**, **Supplementary Fig. S2C-F**). Using this cDNA rescue assay, we found that mutational inactivation of kinase activity ($MARK2^{K82H}$) compromised cancer cell proliferation (**Supplementary Fig. S2G**). We further validated the importance of MARK2/3 catalytic function using a bump-and-hole strategy (50), in which the replacement of endogenous MARK2/3 with $MARK2^{M129G}$ rendered the proliferation of YAPC cells sensitive to the bulky kinase inhibitor 1NM-PP1 (**Fig 1I and Supplementary Fig. S2G**). Collectively, these experiments validated MARK2/3 as catalytic dependencies in specific carcinoma and sarcoma cell line models.

MARK2/3 dependency in cancer is linked to the maintenance of YAP/TAZ function

We next sought to understand why MARK2/3 is essential in some cancer contexts, but dispensable in others. The top mutational correlate of MARK2/3 dependency in our cell line panel was of *KRAS*

(**Supplementary Fig. S3A-B**). However, our validation experiments failed to establish a mechanistic link between MARK2/3 and RAS (**Supplementary Fig. S3C-D**). Using transcriptome analysis, we found that MARK2/3 essentiality across the 31 cancer lines was correlated with the expression of *YAP* and *TAZ* and with the expression of canonical YAP/TAZ target genes *MYOF*, *CYR61*, *DKK1*, and *CAV1* (**Fig. 2A, 2B**) (51-53). Using dual sgRNA vectors, we confirmed that YAP and TAZ function redundantly as dependencies in this cell line panel in a manner that closely correlated with MARK2/3 essentiality (**Fig. 2B, 2C**, **Supplementary Fig. S3E, S3F**). This observation led us to hypothesize that MARK2/3 is critical for maintaining YAP/TAZ function in diverse human cancer contexts. In support of this, we found that the inactivation of MARK2/3 led to reduced expression of a fluorescence-based TEAD:YAP/TAZ reporter in MDA-MB231 cells (**Fig. 2D**) (19). In addition, RNA-seq analysis performed in 20 different cancer cell line models following MARK2/3 knockout demonstrated reduced expression of a YAP/TAZ transcriptional signature in MARK2/3-dependent lines (**Fig. 2E-G**, **Supplementary Table 7**). We extended this analysis by performing genome-wide profiling of active chromatin (H3K27 acetylation), which revealed that MARK2/3 and YAP/TAZ are each critical to activate TEAD4:YAP-bound enhancer elements (**Fig. 2H, 2I, Supplementary Fig. S3G-I**). Together, these results suggest that MARK2/3 are required to maintain the essential function of YAP/TAZ in human cancer.

MARK2/3 catalyze inhibitory phosphorylation of NF2 and activating phosphorylation of YAP/TAZ

Upon inactivating MARK2/3, we observed a striking increase in LATS1/2 T1079/T1041 phosphorylation (**Fig. 3A, 3B, Supplementary Fig. S4A**). This activation mark is known to be catalyzed redundantly by MST1/2 and MAP4K kinases, an activity that is further enhanced by NF2 (**Fig. 3A**) (4). Knockout of MARK2/3 triggered reduced nuclear levels of YAP/TAZ, which is an expected outcome of strengthening LATS1/2 function (**Fig. 3C, Supplementary Fig. S4B, S4C**).

While prior studies have shown that MARK2/3 inhibits the function of MST1/2 (33,49,54), we reasoned that this substrate would be insufficient to account for the MARK2/3 dependency in cancer, since MST1/2 function redundantly with MAP4Ks to regulate YAP/TAZ in human cells (see below) (4,6). This prompted us to perform a broader exploration of MARK2/3 substrates in the Hippo pathway using a chemical-genetic strategy (**Fig. 3D**) (55). Our approach exploited gatekeeper substitutions of MARK2 (M129G) and MARK3 (M132G), which can accommodate bulky ATP-γ-S analogs (e.g. 6-Fu-ATP-γ-S). We co-expressed $MARK2^{M129G}$ or $MARK3^{M132G}$ with 18 different epitope-tagged Hippo pathway components in HEK293T cells, followed by treatment with 6-Fu-ATP-γ-S and immunoprecipitation-western blotting with a phospho-thio-ester-specific antibody. This approach validated the known ability of MARK2/3 to phosphorylate CDC25C and MST1/2, in accord with prior findings (**Fig. 3E**, **Supplementary Fig. S4D, S4E**) (49,56). In addition, we identified NF2, YAP, and, to a lesser extent, TAZ, as MARK2/3 substrates in this system (**Fig. 3E**, **Supplementary Fig. S4D, S4E**). We did not detect MARK2/3-dependent phosphorylation of LATS1/2, but did identify robust phosphorylation of several MAP4K kinases (**Fig. 3E**, **Supplementary Fig. S4D, S4E**). To map the exact sites of phosphorylation, we performed *in vitro* kinase assays with purified MARK2 and each substrate, followed by mass spectrometric peptide quantification (**Supplementary Fig. S4F, S4G**). In these assays, MARK2 catalyzed phosphorylation on serine or threonine residues of NF2 (4 sites), YAP (5 sites), and TAZ (4 sites) (**Fig. 3F-H**, **Supplementary Fig. S5A-K, Supplementary Table 8**). By introducing alanine substitutions of these phosphosites into cDNA constructs, we confirmed the importance of these specific serine/threonine residues for MARK2-dependent phosphorylation in human cells (**Supplementary Fig. S6A-E**). Using mass spectrometry analysis, we also identified sites of MARK2-dependent phosphorylation on MAP4K proteins and MST1/2 (**Supplementary Fig. S6F**), however the known redundancy among these kinases (4) led us to prioritize NF2 and YAP/TAZ for further functional investigation.

Two of the sites of MARK2/3-dependent phosphorylation on NF2 were T230 and S315, which have been reported to inhibit NF2 function (57). To further evaluate this, we used a transfection-based assay in HEK293T cells (4,58), in which NF2 overexpression stimulates p-LATS1/2. We found that co-expression of wild-type MARK2/3, but not a catalytically dead mutant, negated NF2-stimulated LATS1/2 phosphorylation (**Fig. 4A, Supplementary Fig. S6G**). In addition, a phospho-mimetic allele of NF2, in which all four sites of MARK2-dependent phosphorylation are substituted with aspartate, was incapable of triggering LATS1/2 phosphorylation (**Fig. 4B, Supplementary Fig. S6H, S6I**). We also found that MARK2 expression was able to disrupt the physical interaction between NF2 and MAP4K kinases (**Supplementary Fig. S6J**) and block MAP4K4/6- and MST1/2-dependent LATS1 phosphorylation (**Supplementary Fig. S6K-O**) (4). Together, our findings suggest that MARK2/3 can indirectly suppress LATS1/2 activity by phosphorylating upstream components of the Hippo pathway.

We next evaluated the functional importance of YAP/TAZ phosphorylation by MARK2/3. LATS1/2 can sequester YAP/TAZ in the cytoplasm by installing phosphorylation that is recognized by 14-3-3 proteins (59). Owing to the adjacent locations of several MARK2/3 and LATS1/2 substrates on YAP/TAZ (**Fig. 3G, 3H**) (60,61), we hypothesized that MARK2/3-dependent phosphorylation might release YAP/TAZ from 14-3-3-mediated inhibition. To evaluate this, we reconstituted LATS1/2-dependent YAP/TAZ phosphorylation using purified proteins (**Fig. 4C**, **Supplementary Fig. S6P**), which was sufficient to trigger interactions with recombinant 14-3-3ε (**Fig. 4D, 4E**). However, pre-incubation of recombinant YAP or TAZ with MARK2 or MARK3 and ATP eliminated the formation of 14-3-3ε complexes despite the presence of LATS1/2-dependent phosphorylation (**Fig. 4D, 4E, Supplementary Fig. S6Q, S6R**). In accord with these *in vitro* findings, expression of a phospho-mimetic allele of YAP or TAZ, in which serine or threonine substrates of MARK2/3 are mutated to

aspartic acid, eliminated the 14-3-3ε interaction in cellular lysates (**Fig. 4F, 4G, Supplementary Fig. S7A**). Consistent with these findings, this phosphomimetic allele of YAP is present in the nucleus and more active than the wild-type protein (**Supplementary Fig. S7B-F**). Collectively, these functional experiments support that MARK2/3-dependent phosphorylation of YAP/TAZ can interfere with LATS1/2-dependent formation of 14-3-3 complexes.

Regulation of NF2 and YAP accounts for the essential functions of MARK2/3 in human cancer

The biochemical findings above prompted us to perform epistasis experiments evaluating whether dual regulation of NF2 and YAP/TAZ underlies the essential function of MARK2/3 in cancer identified in our paralog screen. As expected, we found that the pharmacological inhibition or double knockout of MST1/2, or its adaptor SAV1, failed to alleviate the MARK2/3 dependency (**Fig. 5A-C, Supplementary Fig. S8A-D**). In contrast, inhibition or double knockout of LATS1/2 resulted in a bypass of MARK2/3 essentiality in four different cancer cell line models (**Fig. 5A-C, Supplementary Fig. S8C, S8D**). In these same models, we found that NF2 knockout or expression of a phosphomimic allele of YAP (YAP^{5D}) partially alleviated the MARK2/3 dependency (**Fig. 5D, 5E, Supplementary Fig. S8E**). Moreover, combining the $NF2^{KO}$/YAP^{5D} genetic alterations led to a nearly complete bypass of MARK2/3 dependency in these contexts, which resembles the effects of inactivating LATS1/2 (**Fig. 5E**). Unexpectedly, knockout of NF2 in MDA-MB-231 cells, a breast cancer cell line harboring a biallelic truncating mutation of *NF2*, alleviated the MARK2/3 dependency (**Supplementary Fig. S9A-C**). However, we found that the truncated NF2 protein present in this cell line (amino acids 1-231) is expressed and retains partial functionality (**Supplementary Fig. S9D, S9E**). Collectively, these results suggest that an essential function of MARK2/3 in cancer is to regulate NF2 and YAP/TAZ, which allows for potent indirect control over the output of LATS1/2.

Inducible expression of a protein-based MARK2/3 inhibitor re-instates Hippo-mediated tumor suppression in organoid and xenograft tumor models

The Hippo pathway activity is known to be modulated by cell culture conditions (19), which motivated us to validate MARK2/3 dependency in tumor models with more physiological extracellular environments. Since selective small-molecule inhibitors of MARK kinases are not available, we developed a catalytic inhibitor of MARK kinase activity that could be expressed in an inducible manner in various tumor models. The EPIYA repeat region of the CagA protein of *H. pylori* was reported to potently and selectively inhibit MARK kinase activity by competing with substrate binding (62,63), a peptide we refer to here as MARK kinase inhibitor (MKI) (**Fig. 6A**). We observed that lentiviral expression of MKI, but not an MKI peptide harboring point mutations that abrogate MARK binding (63), reduced the nuclear levels of YAP/TAZ, reduced NF2/YAP/TAZ phosphorylation, and suppressed the expression of a YAP/TAZ and MARK2/3 transcriptional signatures (**Fig 6B-E, Supplementary Fig. S10A-E**). In addition, the proliferation arrest induced by MKI correlated with the overall sensitivity to MARK2/3 double knockout in a cell line panel and the sensitivity to MKI could be alleviated by over-expressing MARK2 (**Fig. 6C, Supplementary Fig. S10F, S10G**). Our epistasis experiments further indicated that engineering of $NF2^{KO}/YAP^{5D}$ alleviated the sensitivity to MKI-mediated growth (**Fig. 6F**), thus validating MKI as a tool catalytic inhibitor that mimics the biological effects of MARK2/3 double knockout when expressed in cancer cells.

We next engineered a vector that expresses MKI under the control of a doxycycline-inducible promoter, which was introduced into a panel of *YAP*- or *TAZ*-amplified human triple-negative breast cancer or pancreatic cancer organoid cultures (**Fig. 6G**). We next introduced the dox-inducible MKI constructs into T3M-4 cells, a basal-like model of pancreatic cancer, followed by orthotopic transplantation (**Fig. 6H-J**). Upon tumors reaching >200 mm^3, tumor-bearing mice were treated with

dox or vehicle control to induce MKI expression (**Fig. 6H**). Using two different imaging modalities, we found that MKI expression led to a marked inhibition of tumor growth *in vivo* (**Fig. 6K-L and Supplementary Fig. S10H**). Similar results were observed in a subcutaneous YAPC xenograft model (**Supplementary Fig. S10I, S10J**). The findings validate the potent anti-tumor effects of catalytic MARK2/3 inhibition in YAP/TAZ-dependent cancer models.

Discussion

It has been observed that human cancers can be broadly classified based on the status of YAP/TAZ (64). YAP/TAZ^{OFF} tumors tend to be of hematopoietic or neural/neuroendocrine lineages, and in this context transcriptional silencing of YAP/TAZ is required for tumor development (64-66). In contrast, YAP/TAZ are activated in human carcinomas and sarcomas, which is essential for tumorigenesis (64,67). This binary classification has important clinical implications, as YAP/TAZ have powerful effects on several tumor cell characteristics, including epigenetic plasticity and drug sensitivity (15,68). Here, we have exploited the ON vs OFF status of this pathway in a human cancer cell line models to reveal a strict requirement for MARK2/3 catalytic activity to support YAP/TAZ function across a diverse array of human carcinomas and sarcomas. Targeting of MARK2/3 leads to potent inhibition of YAP/TAZ and a severe compromise of tumor cell fitness; phenotypes that can be accounted for by phosphorylation of NF2 and YAP as direct MARK2/3 substrates. Our study positions MARK2/3 as dominant regulators of the human Hippo pathway and as a 'druggable' target in YAP/TAZ-dependent tumors.

Early genetic studies in model organisms implicated the MARK1-4 ortholog Par-1 as a regulator of cell polarity (28,69). Subsequent work in *Drosophila* identified Par-1 as a negative regulator of the Hippo pathway, which influences cell growth phenotypes (33). Despite this early observation, the connection between MARKs and Hippo in human cells has been controversial, with some studies suggesting MARKs can activate (33,49,54) or inhibit (48,70) YAP/TAZ function. Since these prior studies focused on the manipulation of individual MARK kinase genes, we suspect that genetic redundancy between MARK2 and MARK3 concealed the powerful inhibitory influence of human MARK kinases over the Hippo pathway. While our findings are generally consistent with earlier work in *Drosophila* (33), the mechanism by which MARK/Par-1 regulate YAP/TAZ might be distinct in

each organism, with an expansion of upstream and downstream substrates of MARK2/3 in human cells that allow for multi-level control over the output of LATS1/2. Nevertheless, our collective work suggests an ancient linkage between MARK and Hippo during metazoan evolution, which may have emerged to integrate cellular polarity with organ growth and regeneration. While our experiments highlight an important role of NF2 and YAP/TAZ as MARK2/3 substrates, it is likely that other substrates in the Hippo pathway contribute to this regulation as well (e.g. MAP4Ks and MST1/2) (33,49,54).

Prior studies have described small molecules that block the interaction between YAP/TAZ and TEAD transcription factors (24-27,71), which are currently the most developed therapeutic strategy for targeting Hippo-dysregulated cancers (72). While the efficacy of such an approach in human patients has only recently begun to be evaluated in clinical trials (clinicaltrials.gov, NCT04665206, NCT05228015), our work reveals chemical inhibition of MARK2/3 kinase activity as an alternative strategy for eliminating YAP/TAZ-addicted tumor cells. As kinases, there may exist unique opportunities to develop potent and selective MARK2/3 inhibitors by leveraging decades of experience in the pharmaceutical industry in targeting this class of enzymes (73), which would differ from the challenges of modulating a protein-protein interaction (74,75). In addition, by functioning upstream to regulate LATS1/2-mediated control over YAP/TAZ, targeting of MARK2/3 would likely select for distinct resistance mechanisms from drugs targeting the TEAD:YAP/TAZ interaction (76). While the liabilities of each targeting strategy await further description in pre-clinical models and ongoing clinical studies, our study justifies consideration of MARK2/3 as a prominent cancer target in a diverse collection of human carcinomas and sarcomas harboring hyper-active YAP/TAZ function.

One clear clinical opportunity for YAP/TAZ modulation in cancer is in the setting of RAS-mutant cancers. Pre-clinical studies have identified YAP/TAZ hyper-activation as a common strategy used by

315 tumor cells to evade the anti-cancer effects of targeted therapy (27,77-80), a finding well-supported by
316 experiments performed in animal models (77,81,82). Thus, an opportunity may exist to combine
317 inhibitors MARK2/3 and RAS to prolong the survival of cancer patients and prevent acquired drug
318 resistance.

Methods

Cell culture

All cell lines were authenticated using short tandem repeat profiling. The HPAF-II, AsPC-1, PANC-1, MIA PaCa-2, NCI-H1299, A549, NCI-H23, RD, MDA-MB231, NCI-H1048, NCI-H211, NCI-H209, NCI-H1836, NCI-H1436, NCI-H2023, NCI-H1975, NCI-H1703, CHL-1, OCI-AML3, THP-1, HEK-293T and K-562 were purchased from American Type Culture Collection (ATCC). The YAPC, PATU8902, PATU8988T, NOMO-1, HEL, SET-2, RH-30, OCI-AML3 and MOLM13 cell lines were purchased from the "Deutsche Sammlung von Mikroorganismen und Zellkulturen" (DSMZ). The KP2, T3M-4, SUIT-2 and KLM-1 cell lines were purchased from the "Japanese Collection of Research Bioresources Cell Bank" (JCRB). The COR-L311 cell line was purchased from the "European Collection of Authenticated Cell Cultures" (ECACC).

All human cell lines were grown in Roswell Park Memorial Institute (RPMI) medium supplemented with 10% fetal bovine serum (FBS) and 1% penicillin/streptomycin (Gibco), if not otherwise indicated. HEK 293T and MDA-MB231 cells were grown in Dulbecco's Modified Eagle Medium (DMEM) medium. NCI-H209, NCI-H1836, NCI-H1436, NCI-H1048 were grown in HITES medium (DMEM media supplemented with 5% FBS, 1% penicillin/streptomycin, Insulin-Transferrin-Selenium (Gibco), 10 nM Hydrocortisone (Sigma-Aldrich), 10 nM beta-estradiol (Sigma-Aldrich), 10 mM HEPES (Gibco), 2mM L-glutamine (Gibco)). All lentiviral packaging with HEK 293T cells and cancer cell line transduction was performed following standard procedures similar to those previously described (35). For organoid culture transduction, single cells were infected using a spin-infection strategy (800g for 2-4h), before virus removal and replating in Matrigel (Corning). All organoids were grown in growth factor reduced Matrigel. Human patient-derived pancreas- and breast cancer organoids were cultured in specific organoid media as described before (83,84). All cell lines were cultured at 37°C

with 5% CO_2, and were periodically tested negative for *Mycoplasma* contamination. All experiments were performed within 20 passages of thawing of cells.

Protein lysate preparation for Western blotting and immunoblotting

Cells were lysed directly with 2x Laemmli Sample Buffer (BIO-RAD), supplemented with β-mercaptoethanol (Sigma-Aldrich) or in RIPA buffer supplemented with protease inhibitor cocktail (Roche) and Halt Phosphatase inhibitor cocktail (Thermo Fisher). The same total protein amounts or extracts from the same number of cells were loaded into each lane of an SDS-PAGE gel (NuPAGE 4–12% Bis-Tris Protein gels, Thermo Fisher) followed by transfer to a nitrocellulose membrane. Membranes were blocked using 5% non-fat dry milk and washed using TBST following incubation both primary or secondary antibodies. After, membranes were developed with chemiluminescent HRP substrate (Pierce).

Antibodies used in this study are HRP-conjugated secondary antibodies (rabbit cytivia, NA934, 1:5,000 – 1:20,000), HRP-conjugated β-actin (Sigma-Aldrich, A3854, 1:5,000), HA (Roche, 3F10, 1:10,000), Flag (Sigma-Aldrich, A8592, 1:5,000), V5 (Invitrogen, R961-25, 1:5,000), myc (Abcam, ab62928, 1:3,000), GAPDH (Cell Signaling, D16H11, 1:3,000), H3 (Cell Signaling, D1H2, 1:5,000), GST-tag (Cell Signaling, 5475S, 1:3,000) and primary antibodies MARK2 (Abcam, ab133724, 1:1,000), MARK3 (Abcam, ab264285, 1:1,000), YAP (Cell Signaling, D8H1X, 1:1,000), p-YAP/TAZ (S127/S89) (Cell Signaling, D9W2I, 4911, 1:3,000), TAZ (Cell Signaling, E8E9G, D3I6D, 1:1,000), NF2 (Cell Signaling, D1D8, 1:1,000), MST1 (Cell Signaling, 3682T, 1:1,000), MST2 (Cell Signaling, 3952T, 1:1,000), LATS1/2 (GeneTex, GTX87014, 1:1,000), p-LATS1/2 (T1079/T1041) (Cell Signaling, D57D3, Abcam, ab305029, 1:1,000 – 1:3,000), SAV1 (Cell Signaling, D6M6X, 1:1,000), CDC25C (Cell Signaling, 5H9, 1:1,000), p-CDC25C (S216) (Cell Signaling, 63F9, 1:1,000), Thiophosphate ester (Abcam, ab92570, 1:5,000 – 1:20,000), 14-3-3 (Cell Signaling, 8312S, 1:1,000),

ERK (Cell Signaling, 137F5, 1:1,000), p-ERK (Cell Signaling, D13.14.4E, 1:1,000). Immunohistochemistry: GFP (Abcam, 6673, 1:500). Immunofluorescence: anti-HA (Cell Signaling, 3724, 1:400), anti-α-Tubulin−FITC (Sigma-Aldrich, F2168, 1:400)

Immunohistochemistry

Tumor tissue was fixed in paraformaldehyde and embedded in paraffin. Paraffin was removed and tissue was dehydrated following which antigen was retrieved by boiling in an EDTA (1mM), TRIS buffer (10mM, pH: 9.0). Tissue was blocked with 5% BSA-TBS-T and incubated with GFP antibody (1:500) overnight, washed with TBS-T and stained with HRP conjugated secondary antibody (1:400), before development with 3,3′-Diaminobenzidine (DAB) and counterstain with hematoxylin.

Immunofluorescence imaging

Six days after double knockout A549 (25,000 cells/well) were seeded on poly-L-lysine coated 4 well µ-slide (Ibidi). After 24h fixed (10% neutralized formalin) for 10 minutes. Cells were permeabilized with 0.5% Triton X-100/PBS for 10 minutes and washed twice with wash buffer (0.1% BSA/1xPBS). After, cells were incubated with blocking buffer (10% normal goat serum (Invitrogen) + 0.3% Triton X-100) for 45 minutes. Primary antibodies were diluted with dilution buffer (1xPBS, 1%BSA, 1% normal goat serum, 0.3% Triton X-100, 0.01% sodium azide) and added after blocking. Slides were incubated at 4°C overnight. Cells were washed twice with wash buffer and probed with Alexa Fluor 647-conjugated secondary antibody (Goat anti-Rabbit IgG (H+L) Highly Cross-Adsorbed Secondary Antibody, Alexa Fluor 647, 1:1000, Invitrogen, A21245) for one hour at room temperature. Cells were washed twice with wash buffer and nuclear counterstaining was performed by adding mounting media with DAPI (ibidi). For starvation assay, 25k per well of transfected 293T cells were seeded on Collagen I coated Culture Slide (Corning). After 24 hours of incubation with serum-free media, cells were treated with FBS-containing media for two hours. Images were collected with 40X/1.10 HC PL

APO water immersion objective lens using Leica TCS SP8 laser scanning confocal microscope and were processed with Leica LAS X software. For 3D quantification, z-stacks of the specimen were acquired with a slice interval of 0.5µm. Three z-stacks were taken in three biological replicates each and were analyzed by IMARIS software (10.1.1, Oxford Instrument). Nuclear and cytoplasmic volumes and mean YAP intensity were calculated by the Surface function in Imaris. 3D reconstructed surfaces were created around blue (DAPI) or red (YAP) signals and the thresholding cut-off was optimized based on the fluorescence intensity of each fluorescence channel. After 3D surface reconstructions were optimized, we imported DAPI and YAP surfaces to the Imaris Cell Biologist module to compartmentalize the YAP signal to associated cytoplasm or nuclei. To ensure consistency in intensity data measurements within and between, consistent imaging and analysis parameters were applied to all the images.

Apoptosis and cell cycle analysis using flow cytometry

For Apoptosis analysis cancer cells transduced with sgRNA constructs were stained using conjugated Annexin-V proteins (Thermo Fisher Scientific) and DAPI according to manufacturer instructions. In brief, 6 days post-infection with lentivirus containing dgRNAs linked to GFP, Cells were detached and resuspended in staining buffer followed by incubation with Annexin-V and DAPI. Stained cells were analyzed by flow cytometry and data analysis was performed with FlowJo software. Early apoptotic- (Annexin-V^+/$DAPI^-$), late apoptotic- (Annexin-V^+/$DAPI^+$), necrotic- (Annexin-V^-/$DAPI^+$) and viable cells (Annexin-V^-/$DAPI^-$) were identified.

For cell cycle analysis cancer cells transduced with dgRNA constructs (day 5) were treated with 10µM EdU 4h prior to sampling. EdU incorporated into cells was stained according to manufacturer instructions (Thermo Fisher). In brief, Cells were detached and fixed in 4% PFA, permeabilized and EdU conjugated using click chemistry. Stained cells were analyzed by flow cytometry and data

analysis was performed with FlowJo software. Cells were identified based on EdU signal and DNA content (DAPI).

CRISPR screening and pooled paralog library generation.

Library generation

The Paralog co-targeting CRISPR library was optimized for the use of SpCas9, a system we recently published(85). Oligonucleotide pools (n=64,697) double guide RNAs targeting 1,719 single gene and 2,529 gene combinations were synthesized (Twist Bioscience) with BsmBI cutting sites in between overhang sequences for the dual crRNA fragment. Primers matching the overhang for the lentiviral backbone were used to amplify the oligonucleotide pools. PCR products were purified and cloned using Gibson assembly master mix (New England BioLabs) into LRG3.0, a lentiviral vector with human U6 and bovine U6 promoters expressing the two sgRNAs in inverse orientation. To incorporate the dual tracrRNA, the purified tracrRNA fragment was cloned in between the dual crRNAs by a second round of Gibson assembly.

Paralog library screening

To generate stable cell lines, cells were first transduced with a Cas9 vector (Addgene: 108100). Next, cell lines were transduced with the paralog co-targeting CRISPR library virus aiming for a representation of 1,000 cells per sgRNA at a low multiplicity of infection (MOI ~0.3). Briefly, cell lines were transduced by spin infection for 45 min at 600g. On day 3, an initial sample was taken and cells were re-plated maintaining representation. Once 10 cell doublings were reached samples for genomic DNA extraction were again taken.

Genomic DNA extraction

Cells lysed in extraction buffer (10mM Tris, 150mM NaCl, 10mM EDTA, Proteinase K (0.02mg/mL), SDS (0.1%)). Lysates were incubated at 56°C for 48h and genomic DNA was extracted using TRIS-saturated phenol (Thermo Fisher Scientific).

dgRNA PCR for Illumina sequencing

DNA was PCR-amplified and barcoded with P5/P7 primers (Integrated DNA Technologies) using Taq-Gold DNA polymerase (Thermofisher) according to the manufacturer's instructions. Briefly, Taq polymerase, reaction buffer, Magnesium chloride, primers, and 1µg of genomic DNA were mixed and used for each reaction (round 1: PCR for 11 cycles). Amplified DNA was size selected (200-300bp) and barcoded in a second round PCR using stacked P5/P7 primers (round 2: PCR for 9 cycles). The PCR product was sequenced using a paired-end 75 base pair (bp) reads protocol (Illumina).

Calculation of paralog CRISPR screening $\log_2$(fold-change), synergy, P value and FDR

Reads were counted by mapping dgRNA sequences to the reference file of the library and a pseudo count of 16 was added. To systematically calculate the degree of phenotypic synergy or epistasis between two paralog knockouts we utilized GEMINI, a variational Bayesian approach to identify genetic interactions in CRISPR screening data (43). The GEMINI R (v.1.4.0) package was used to calculate $\log_2$(fold-changes) (LFC) and synergy scores and statistics with their corresponding P and FDR values (Supplementary Table 2,4-6). GEMINI calculates the LFC of the dgRNA abundance between initial time point (average abundance of dgRNAs day3 n=10) and the 10-doubling time endpoint. GEMINI has been used to compute the synergy score by comparing the LFCs of each gene pair to the most lethal individual gene of the pair. Non-synergistic pairs were used to calculate FDR and P value. Bayesian analysis and the prior choice were performed as described previously (43).

Variance of averaged log2 fold-change dgRNA abundance was calculated by averaging the squared deviations of a double knockout log2 fold-change.

$$Variance = \frac{\sum(x - \bar{x}_{average})^2}{(n-1)}$$

Paralog gene identification and functional domain mapping

Paralog pairs were identified by aligning human proteome (>100,000 amino acid sequences) using the Basic Local Alignment Search Tool (BLAST). Matches originating from the same gene were removed. Each top-scored paralog-pair identified (*E* value < 0.01), that shared the same functional domain of interest was included in the Paralog library. In addition, high-scoring paralogs (*E* value < 10^{-100}) were included. Functional domains were mapped using Reverse Position-Specific BLAST and the conserved domain database (CDD) (86).

Selection of sgRNAs and controls

Domain annotation and sgRNA positions were compared and sgRNAs cutting in functional domain regions were included in the sgRNA selection pool. sgRNAs with off-targets in paralog genes were removed from the selection pool. Additionally, sgRNAs incompatible with the cloning strategy were removed from the selection pool. sgRNAs were picked based on their off-target score (calculated based on the number of off-target locations in the human genome factored by the fall-off in cutting-efficiency of spCas9 in case of crRNA sequence miss-match). For each gene, 3-4 selective domain-focused sgRNA were picked and combined. A set of sgRNAs targeting known essential genes as positive controls (n=28) and a set of non-targeting (n=97) as well as non-coding region targeting negative controls (n=54) were included in the library. To construct cell line-specific negative controls (non-synergistic pairs), we selected genes that were not expressed in a cell line according to the RNA-seq data ($\log2(TPM + 1) < 0.1$).

Arrayed GFP competition assays

For validation, two sgRNAs were synthesized together with bovine U6 promoter as gene blocks (Integrated DNA Technologies) and cloned using Gibson assembly into LRG2.1T (Addgene, 65656). All inserts were verified by Sanger sequencing (Eurofins Genomics). To generate LATS1/2 and MST1/2 double knockout pools two sgRNAs co-targeting LATS1/2 or MST1/2 were combined and two sgRNA targeting SAV1, NF2 were combined on one vector. For lentivirus packaging, HEK 293T cells were transfected with sgRNA, pVSVg, psPAX2 plasmids (Addgene, 12260) using PEI reagent (PEI 25000). Percent GFP^+ populations were followed over time after infection using the Guava Easycyte flow HT instrument (Millipore). Complete sgRNA sequences are given in Supplementary Table 9.

Generation of ectopic overexpression vectors

All cDNAs were either cloned from Addgene plasmids or synthesized as indicated below. CRISPR-resistant cDNAs were generated either by mutating the PAM sequence or sgRNA binding sites into synonymous codons. All cDNAs were cloned into lentiviral constructs derived from LentiV (Addgene 108100), altered to contain internal ribosome entry site (IRES) elements and selection marker resistance genes. For doxycycline induction of cDNA expression, genes were cloned into Doxi-LentiV (derived from Addgene, 80921, 89180 and 71782) vectors and expression was induced using 2 μg/ml doxycycline. MARK1, MARK2, MARK3 and MARK4 (Addgene, 170582, 23404, 23716) (ORIGENE: SC107258), were cloned into the LentiV-IRES vector after the addition of a Flag tag at the N terminus. Hippo pathway genes- LATS1, LATS2, NF2, SAV1, TAZ, MOB1A, MOB1B, MST1, MST2, TEAD1, YAP, YAP mutants, TAZ mutants, MST1 mutants, GFP, CDC25C and YWHAE (14-3-3ε) encoding V5, HA or myc-tagged cDNAs were from Addgene (66851, 66852, 32834, 32836, 32839) or synthesized (IDT). cDNA encoding for MAP4K1, MAPK4K2, MAPK4K3, MAPK4K4, MAPK4K5, and MAPK4K6, were from Addgene (23484, 23644, 23664, 23486, 23611, 23522) 3xHA

514 tagged and cloned into LentiV. The MAPK4K7, MAP4K4^{10A} and MAP4K4^{10D} expression vector was
515 generated by Vector Builder. All mutations were introduced by geneBlock synthesis or PCR. MKI^{WT}
516 was derived from the coding sequence of CagA (*H.pylori* strain 26695). The sequence containing the
517 EPIYA-repeat regions amino acid position 885-1105 was codon optimized. The cDNA was
518 synthesized and cloned into LentiVi-P2A-GFP or Doxi-LentiV after the addition of a 3xHA or Flag tag
519 at the N terminus. To generate a mutant of MKI with impaired MARK binding capacity (MKI^{MUT}) the
520 leucine 109/143 in the two MARK binding motifs of MKI^{WT} were mutated to glycine.
521
522 Generation of TEAD binding reporter linked to GFP
523 To generate a TEAD-driven GFP reporter, the promoter of the established TEAD binding reporter
524 (8xGTIIC)(19) (Addgene, 34615) was fused into a construct containing destabilized GFP (Addgene,
525 138152).
526
527 Generation of clonal analog sensitive YAPC cells for growth assays
528 MARK2 analog-sensitive mutants were generated by mutating the gatekeeper amino acid methionine
529 129 to glycine. The functionality of this mutant was confirmed using rescue assays. YAPC cells were
530 infected with cDNA CRISPR resistant to sgMARK2+3 and 3 single cell clones were picked. Mutation
531 of endogenous MARK2 and MARK3 locus for all clones was confirmed using genotyping methods
532 (PCR and nanopore sequencing).
533
534 Cloning, expression, and purification of recombinant proteins
535 ORF encoding human MARK2 (Addgene, 23404) was cloned into pFL system with an N-terminal
536 Strep2SUMO tag. Bacmid was generated using pFL vector using DH10MultiBac cells (Geneva
537 Biotech). Sf9 cells were transfected with purified bacmids. Cells were lysed and rMARK2 was purified
538 using StrepTactin Super flow resin. Protein was aliquoted and snap-frozen at -80°C. Protein

concentration was estimated by measuring Abs_{280nm} and samples were assessed by Coomassie staining and MS analysis, confirming the absence of other protein kinases. Recombinant LATS1, LATS2, MARK3 and 14-3-3ε were purchased (Active Motif, 81209, Signalchem, L02-11G, M45-10G, Y75-30H) and purity, correct protein size was confirmed by Coomassie staining.

Human ORFs encoding YAP and TAZ were cloned into pGEX4T1 vector with N-terminal GST-tag. BL21-CodonPlus (DE3)-RIPL competent cells (Agilent, 230280) are transformed with sequence-validated vectors. Protein expression was induced with IPTG (GoldBio, I2481C) at 16°C for 18 hours. Bacteria were sedimented, lysed, sonicated and cleared lysates were loaded, washed followed by elution using (50 mM Tris pH 8, 300 mM NaCl, 10% glycerol, 20 mM reduced L-glutathione). Purified proteins were aliquoted and flash-frozen at -80°C. The purity of the proteins was assessed by Coomassie staining. Protein concentration was estimated through Abs_{280nm} measurements.

<u>In-cell phosphosubstrate identification</u>

Gatekeeper mutant $MARK2^{M129G}$ or $MARK3^{M132G}$ cDNA was co-transfected together with cDNAs of individual genes into HEK 293T using polyethyleneimine (PEI). After 24h cells were harvested and incubated for 30 min at 30°C in bulky-ATP-analog (N^6-Furfuryl-ATP-γ-S) containing Kinase-labeling buffer (Protease inhibitor, 20 mM HEPES, 100 mM potassium acetate, 5mM sodium acetate, 2mM magnesium acetate, 10 mM magnesium chloride, 1mM EGTA, 45 µg/mL Digitonin, 0.5 mM TCEP, 5mM GTP, 600 µM ATP, 75 µM N^6- Furfuryl-ATP-γ-S). Cells were lysed using RIPA buffer (with the addition of 0.1% SDS and 250 U/mL Benzonase). Thiophosphorylated substrates were alkylated using 2.5 mM para-nitrobenzyl mesylate (PNBM) for 10min at RT. Target proteins were affinity purified and analyzed using western blot and anti-thiophosphate ester-specific antibodies.

Identification of phosphosites using mass spectrometry (MS) and phosphoproteomics.

Sample preparation and MS recording

Substrate cDNAs were transfected into HEK 293T as described above and sampled 24 h after transfection. Samples were affinity purified using HA-agarose beads (Sigma-Aldrich) and treated with 800 U of Lambda Phosphates (New England Biolabs) for 30 min at 30°C. Beads were washed with RIPA buffer (with Protease inhibitor and Phosphatase inhibitor cocktails). Next, beads bound proteins were incubated for 30min at 30 °C with 3 µg rMARK2 in Kinase-buffer (Tris-HCl pH=7.5, 5 mM MgCl2, 2 mM EGTA, 0.5 mM DTT, 100 µM ATP, Protease- and Phosphatase inhibitor cocktail). Phosphorylated substrates and negative controls were resolved by SDS-PAGE and proteins were stained with Coomassie blue. The bands corresponding to each putative substrate were excised, and gel bands were de-stained. After irreversible alkylation of Cysteine residues, proteins were digested with Trypsin, and peptides were analyzed by LC-MS/MS. Peptides were resolved by nanoscale reversed-phase chromatography and ionized by electrospray (2,200V) into a quadrupole-orbitrap mass spectrometer (Thermo Exploris 480). The MS was set to collect 120,000 resolution precursor scans before data-dependent HCD fragmentation and collection of MS/MS spectra. The area under the curve for chromatographic peaks of precursor peptide ions was used as quantitative metrics for label-free quantification.

Identification of phosphosites

Raw files were analyzed using the Proteome Discoverer environment. For peptide identification, spectra were matched against the UniProt human sequence database, supplemented with common contaminants from the cRAP database and with the sequences of the recombinant proteins expressed as substrates. S/T/Y phosphorylation, N/Q deamidation, and M oxidations were set as variable modifications. Alkylation of C residues with CEMTS was set a static modification. Up to 3 missed trypsin cleavages were allowed. Peptide-spectral matches were filtered using Percolator to maintain

1% FDR using the target-decoy method. The area under the curve defined by peptide ion XIC was integrated and used as a quantitative metric for label-free quantification. To evaluate differential phosphorylation in MARK2-treated samples compared to controls, peptides from each putative substrate were parsed out, and label-free quantification (LFQ) AUC values were used as metrics for relative chemical isoform abundance across conditions. Peptides with no LFQ value in any of the samples were disregarded. For peptides only quantified in one experimental arm, the missing value was imputed using a value smaller than the smallest empirical LFQ in the dataset (value chosen as a proxy for LFQ at detection limit). Relative amounts of phosphorylated peptides in MARK2 treated and control samples were assessed for each chemical isoform independently. Phosphopeptides that were either specifically detected in the MARK2 treated samples or showing differential abundance across conditions (>2-fold-change in MARK2 treated vs untreated sample) and whose identity could be confirmed by manual spectral interpretation were prioritized for further validation using in-cell phosphosubstrate identification strategy described above. The fragmentation spectra supporting peptide identity and phosphorylation localization together with the extracted precursor ion chromatogram (XIC) can be found in Supplementary material.

Crystal violet staining

Cas9-expressing cancer cells were infected with lentivirus. After 3 days GFP percentage was determined using flow cytometry. GFP^+ cells were seeded into 24 well plates at a density of 5,000/well. Cells were selected and grown for 10-12 days in the presence of 10µg/mL Blasticidin for controls to reach near confluency. Media was changed every 3 days. Cells were fixed using 4% paraformaldehyde for 15 min followed by staining with Crystal violet (1mg/mL in 90/10% Water/Ethanol) for 5 min. Wells were washed 4 times with water and plates were imaged.

Subcellular fractionation assay

Following perturbation, cancer cells were treated with 500µM cytosolic extraction buffer (10mM HEPES, 10mM KCl, 1mM DTT, 0.1 mM EDTA, 0.1mM EGTA) for 10min on ice. Cells were vortexed for 10sec after the addition of NP40 (final 0.65%) to allow hypotonic cell membrane lysis, followed by 5 min 1,500 g centrifugation at 4°C. Cytosolic fraction was removed and pelleted nuclei were lysed in RIPA buffer supplemented with 250 U/mL Benzonase and Protease- and Phosphatase inhibitor cocktail.

Co-Immunoprecipitation assays

HEK 293T cells were transfected with vectors expressing myc-LATS1, myc-LATS2, V5-14-3-3 or V5-NF2 together with Flag-MARK2, Flag-MARK2^{K82H} or Flag-MARK3 and wild-type or mutant HA-tagged substrate cDNAs. For immunoprecipitation, cells were lysed in NP40 buffer (20 mM of Tris-HCl, 100 mM of NaCl, 1% NP40, 2 mM of EDTA, Protease- and Phosphatase inhibitor cocktail) or RIPA buffer (Thermo Fisher Scientific) for 10 min at 4 °C. Protein lysates were then centrifuged at 13,000g for 15 min at 4 °C. The supernatant was then transferred to new collection tubes and incubated with to 30 µl of prewashed anti-myc or -V5 beads (Chromotek) and equilibrated to a final volume of 1000 µl by adding lysis buffer. Precipitation was performed at 4 °C overnight and washed 4-5 times with lysis buffer. Samples were eluted by boiling for 10 min in 2x Laemmli Sample Buffer supplemented with β-mercaptoethanol.

In vitro phosphorylation and interaction assay

Bacterial purified recombinant GST-YAP or GST-TAZ were pre-incubated for 30min at 30 °C with recombinant MARK2 or MARK3 in Kinase buffer followed by incubation with either recombinant LATS1 or LATS2 for an additional 30min. Phosphorylated YAP or TAZ were then incubated with 6xHis-14-3-3 bound to Ni-NTA affinity resin for 4-16h followed by washing and samples elution.

638 In vitro phosphorylation of synthetic peptides

639 A peptide sequence around S127/S128 of YAP was used and charge-stabilized by adding arginine at
640 the C-terminal end (ALTPQHVRAHSSPASLQLGAVR). Peptide was synthesized with or without
641 phosphorylation at S128, S127/S128. 400ng of LATS2 and 1µg of peptide were incubated in Kinase
642 buffer (Tris-HCl pH=7.5, 5 mM MgCl2, 2 mM EGTA, 0.5 mM DTT, 100 µM ATP, Protease- and
643 Phosphatase inhibitor cocktail) and peptides were prepared and analyzed using mass spectrometry as
644 described above.

645

646 qPCR and RNA-extraction

647 Total RNA was extracted using TRIzol™ (Thermo Fisher) followed by cDNA synthesis (Quantabio)
648 following manufacturer instructions. Briefly, cells were lysed using 1mL TRIzol™ followed by
649 Chloroform addition and isopropanol/ethanol precipitation. cDNA synthesis of 1µg of total RNA using
650 the recommended thermocycler program (5min 25°C, 30min 42°C, 5min 85°C). For qPCR
651 PowerSYBR Green PCR Master mix (Thermo Fisher) was used. 1µL of cDNA template per reaction
652 was added to 5µL of master mix and 0.5µM primer, followed by triplicate PCR. Ct values were
653 calculated for each primer pair, normalized to GAPDH and HPRT, and differential MAR2 expression
654 (ΔΔCt) in sgMARK2 samples was quantified compared to sgControl.

655

656 RNA-seq, CUT&RUN sample preparation and library construction

657 For RNA-Seq libraries, total RNA was prepared using TRIzol reagent according to the manufacturer's
658 protocol (Thermo Fisher Scientific). Libraries were constructed with the TruSeq Sample Prep Kit v2
659 (Illumina) following the manufacturer's protocol. Briefly, 2 µg of total RNA was used for Poly-A
660 enrichment, fragmentation, cDNA synthesis, end repairing, A tailing, adapter ligation and library
661 amplification. For CUT&RUN, antibody-guided DNA cleavage was performed using the CUTANA

CUT&RUN kit (EpiCyper) according to the manufacturer's instructions. Briefly, 500,000 knockout cells were crosslinked for 1 min using 1% paraformaldehyde (PFA) and quenched using Glycine for min. Pre-washing buffer was used with detergents (0.05% SDS and 0.2% Triton X-100). Antibodies used were H3K27ac and IgG (EpiCyper, 13-0045;13-0042). Libraries were constructed with the NEBNext Ultra II DNA Library Prep Kit (New England BioLabs) following the manufacturer's low DNA protocol. Briefly, complete CUT&RUN DNA extracts were spiked-in with E. coli DNA fragments and subjected to end repair, A tailing and adapter ligation (at 1/25 dilution) followed by PCR amplification. Libraries were purified using AMPureXP beads before and after PCR. Barcoded libraries were sequenced using an Illumina Nextseq.

Bioinformatics- Mutational analysis, RNA-seq, GSEA, ChIP-seq analysis

Basal expression levels, copy number variations and mutations

For cell lines basal expression data (TPM) and copy number variations (CNV) absolute values from the cancer cell line encyclopedia (CCLE) (87) were used. RNA-seq data for KLM-1 was obtained from GSE140484. Mutational information from both the CCLE and Cosmic databases was used (88). TNBC and PDAC organoid CNV data were previously published (83,84). Normalized "The Genotype-Tissue Expression" (GTEx) data were downloaded from "the human protein atlas" (89). Mutational analysis was performed using the custom analysis tool of the Depmap portal (https://depmap.org/portal/), using both hot spot and damaging mutations. Effect sizes and *P* values were calculated using the linear association model with shrinkage correction (https://github.com/broadinstitute/cdsr_models/blob/master/R/linear_association.R).

RNA-Seq analysis

Raw reads were pseudo-aligned to the transcriptome of the human genome (hg38) using Kallisto (90) with bootstrap 100. For differential gene expression analysis, pseudoalignment counts were read into

DESeq2, comparing samples vs control ($Ctrl^{KO}$) with two replicates for each sample. The differential expression gene analysis was performed using a gene expression cutoff of >0.5 TPM. Results from multiple sequencing runs were batch-corrected using the R package (sva), before count normalization, transformation, and z-score calculation. For heatmap, z-scores of normalized counts from significantly (adjusted P value < 10^{-4}) down or up-regulated (log_2(fold-change) < -1 or > 2) genes in MARK2+3^{dKO} condition were used and plotted using R package (ComplexHeatmap).

Generation of YAP/TAZ gene signature and gene set enrichment analysis (GSEA)

The differential gene expression gene lists of YAP+TAZ^{dKO} compared to $Ctrl^{KO}$ were ranked and the top 200 downregulated genes in YAP+TAZ^{dKO} condition were combined. Gene counts were ranked and genes found in at least 1/3 of models were used to generate a general cancer cell line YAP/TAZ target gene set (n=43) (Supplementary Table 7). Differentially expressed gene lists were further analyzed using gene set enrichment analysis with a weighted GSEA Pre-ranked tool. 1,000 gene set permutations were applied(93) and the common cancer YAP/TAZ target gene set was used to analyze the effects of sgMARK2/3 double guide RNAs on gene expression. All fold-changes are provided in Supplementary Table 10A,10B.

CUT&RUN and ChIP-seq analysis

Raw reads were aligned to the human genome (hg19) and *E.coli* genome (K12) using Bowtie2 software in sensitive mode(91). Duplicate reads were removed before peak calling. Deeptools was used to normalize samples to *E.coli*-DNA spike-in controls. Peaks were identified using MACS2 software (92) using 5% FDR cut-off and broad peak option for histone or narrow peak option for transcription factor-ChIP-seq datasets. H3K27ac peaks identified from $Ctrl^{KO}$ and MARK2+3^{dKO}, YAP+TAZ^{dKO} samples were merged and overlapping peaks were combined. Normalized tag counts were calculated using the Bamliquidator package (https://github. com/BradnerLab/pipeline) without

read extension and log_2(fold-change) between control and dKO samples was calculated for each peak. YAP/TAZ sensitive enhancers were defined by bound by H3K27ac signal reduction (-1.5 > log_2(fold-change)) and binding of YAP and TEAD4 in ChIP-seq (only enhancers with relative tag count >3 in Ctrl samples were used; n=7,896; Supplementary Table 11).

ChIP-seq datasets of TEAD4 and YAP from MDAMB231 cells were obtained from public GEO data sets TEAD4 and YAP (GSE66081). Sequencing depth normalized ChIP-seq and CUT&RUN pileup tracks were generated using the UCSC genome browser.

In vivo tumor growth assay

For tumor growth models, cells were injected into the left or right flank. For inducible MARK inhibition experiments *in vivo*, $1x10^5$ TRE3G-MKI$^{WT/MUT}$-PGK-rtTA3 cancer cells in 100µL growth factor reduced Matrigel were transplanted subcutaneously into the left or right flank of NOD.Cg-Prkdc^{scid} Il2rg^{tm1Wjl}/SzJ (NSG) mice. Animals were treated with doxycycline in drinking water (2 mg/ml with 2% sucrose; Sigma-Aldrich) to induce MKI protein expression. For stable knockout experiments *in vivo*, YAPC cells were transduced with (hU6-sgRNA-bU6-sgRNA)-EFS-GFP-2A-BlastR lentivirus, followed by selection with Blasticidin for 3 days. After, $1x10^5$ GFP$^+$ viable cells were transplanted subcutaneously in 100µL growth factor reduced Matrigel into the right flank of NSG mice. For all subcutaneous xenograft experiments tumor growth was monitored using caliper measurements. Volume was calculated as described previously (94).

For orthotopic transplantation, $5x10^4$ TRE3G-MKI^{WT}-PGK-rtTA3, EFS-LUC-2A-NIS T3M-4 cancer cells were injected into the pancreas of NSG mice. Tumor growth was followed by monitored bioluminescence imaging. Animals were treated with doxycycline in drinking water (2 mg/ml with 2% sucrose) and food (625 mg/kg) to induce MKI protein expression. *In vivo* bioluminescence images

were acquired with an IVIS Spectrum scanner and Living Image software (Revvity). Images were acquired with an open filter on platform D, 12 minutes after a 200 µl intraperitoneal (IP) injection of 15 mg/ml D-Luciferin (Goldbio). Mice were anesthetized with 1.5 to 2% isoflurane in air for the duration of the scan. Due to the motile nature (and variable tissue depth) of the pancreas, four views of each mouse were acquired at each imaging timepoint; dorsal, left flank, ventral and right flank. The amount of emitted light was then quantified as "radiance (photons)", as p/sec/cm^2 /sr from all four views, again using Living Image software. The sum of these 4 views was then made, before graphing as a single data point. *In vivo* NIS-SPECT images were acquired on a Mediso nanoScan SPECT/CT scanner (Mediso USA). Mice were injected subcutaneously with a nominal activity of 45 MBq [^{99m}Tc]sodium-pertechnetate, diluted in saline to a volume of 100 µl. After 50 minutes of conscious uptake, mice were anesthetized with 3% isoflurane in oxygen, weighed and placed on a Mediso double mouse imaging cradle that monitored respiration rate and maintained body temperature with circulating warm air. Lubricating ophthalmic ointment was applied and 1 – 2% isoflurane anesthesia was maintained for the duration of the scan. A CT scan (360 projections at 50 kVp and 112 µAs exposure) was first acquired for anatomical reference and attenuation correction. A whole-body SPECT scan with pinhole collimators was then acquired 60 minutes after [^{99m}Tc]sodium-pertechnetate injection (total SPECT scan time 23 minutes). CT images were reconstructed using filtered back projection with a cosine filter to a voxel size of 250 µm isotropic. SPECT images were reconstructed using a 3D iterative algorithm optimized for high dynamic range with 48 iterations and three subsets to a 128x128 matrix with a 390 µm isotropic voxel size. Attenuation, decay and scatter corrections were applied. SPECT/CT images were processed and analyzed with VivoQuant 4.0 software (inviCRO, Boston, Massachusetts) as described previously (10). Briefly, SPECT images were converted to units of SUV, and an arbitrary threshold of 5 SUV was applied to highlight regions of increased uptake. The stomach and other sites of endogenous pertechnetate uptake were manually removed from the threshold region, and the remaining viable tumor volume was quantified. Additionally, the tumor

762 volume was calculated by manually segmenting a tumor ROI off the CT images. The humane study
763 end-point was determined as the control group's average tumor size reaching > 600 mm^3 or individual
764 tumor size > 2cm diameter.
765
766 Proliferation, viability assay
767 For the proliferation assays, cells were seeded at a density of 500 cells per well into 96-well plates.
768 Cells were treated 24h after seeding and cell viability was assessed 5 days after treatment using the
769 Cell Titer-Glo luminescent cell viability assay (Promega). Cells treated with vehicle control DMSO
770 (0.1%) or killing control 10μM proteasome inhibitor (MG132). Percent viability was calculated by
771 normalizing RLU to DMSO (0.1%) after subtraction of killing control MG132 (10μM) signal.
772 For organoids, 5,000 or 10,000 cells were seeded in a 10% Matrigel/90% organoid media mix and
773 grown for 10 days in the presence or absence of 2μg/mL doxycycline, before assessment of viability
774 using the Cell Titer-Glo luminescent cell viability assay (Promega).
775
776 Animal studies
777 All mouse experiments were approved by the Cold Spring Harbor Animal Care and Use Committee.
778 Animals were treated with doxycycline in drinking water (2 mg/ml with 1% sucrose; Sigma-Aldrich)
779 to induce cDNA expression.
780
781 Data and Code availability
782 Genomic datasets are available from the GEO database under accession code GSE242517. The mass
783 spectrometry proteomics data have been deposited to the ProteomeXchange Consortium via the PRIDE
784 partner repository with the dataset identifier PXD044829. KLM-1 dataset was obtained from
785 GSE140484. ChIP-seq data (YAP and TEAD4) were obtained from GSE66083. Cell line datasets from
786 CCLE (expression as well as mutations and CNV data) were obtained online

(https://depmap.org/portal/download/). Other Data supporting these findings are available in the manuscript and supplementary data. Codes used in generating figures and analyzing the data will be available at: https://doi.org/10.5281/zenodo.10042504

Contributions and Acknowledgements

O.K. and C.R.V. conceived this project and wrote the manuscript with input from all of the authors. O.K. and C.R.V. designed the experiments. O.K. performed experiments with help from D.S., C.T., A.A, F.M., D.A., T.Y. and S.R.. O.K and T.H., performed statistical analysis. T.L.W. and T.Y. performed Immunofluorescence imaging and analysis. O.K. and O.E.D. designed CRISPR sgRNAs. O.K. designed and cloned paralog co-targeting CRISPR libraries. O.K. and D.S. screened libraries in cancer cell lines. O.K., C.T., S.K.L., A.M.C., M.R.J., conducted all xenograft imaging experiments. A.A. generated recombinant MARK2 proteins. F.M. and O.K. performed mass spectrometry sample preparations. M.C.P., F.M. and P.C. performed all mass spectrometry measurements. D.A., S.R. and O.K. performed organoid experiments. C.R.V., D.A.T., P.C., S.K.L., and D.L.S. supervised the studies and acquired funding.

Funding:

This work was supported by Cold Spring Harbor Laboratory NCI Cancer Center Support grant P30-CA045508. Additional funding was provided to C.R.V. by the Pershing Square Sohn Cancer Research Alliance, Simons Foundation, Thompson Foundation, NIH grants CA013106, CA245859, CA229699, as well as support from the Christina Renna Foundation, The Mary Ruchalski Foundation, Friends of T.J. Foundation, Michelle Paternoster Foundation, Daniela Conte Foundation, and Maddie's Promise Foundation. D.L.S. was supported by NCI 2P01CA013106 and CSHL/Northwell Health. O.K. was

supported by Deutsche Forschungsgemeinschaft (DFG) Research Fellowship (KL 3228/1-1). D.A.T. was supported by the Lustgarten Foundation, Simons Foundation, Thompson Foundation, the Pershing Square Foundation, the Cold Spring Harbor Laboratory and Northwell Health Affiliation, the Northwell Health Tissue Donation Program, the Cold Spring Harbor Laboratory Association, and the National Institutes of Health (CA45508, CA210240, CA224013, CA188134, and CA190092).

References

1. Ma S, Meng Z, Chen R, Guan KL. The Hippo Pathway: Biology and Pathophysiology. Annu Rev Biochem **2019**;88:577-604 doi 10.1146/annurev-biochem-013118-111829.
2. Zhao B, Wei X, Li W, Udan RS, Yang Q, Kim J, *et al.* Inactivation of YAP oncoprotein by the Hippo pathway is involved in cell contact inhibition and tissue growth control. Genes Dev **2007**;21(21):2747-61 doi 10.1101/gad.1602907.
3. Huang J, Wu S, Barrera J, Matthews K, Pan D. The Hippo signaling pathway coordinately regulates cell proliferation and apoptosis by inactivating Yorkie, the Drosophila Homolog of YAP. Cell **2005**;122(3):421-34 doi 10.1016/j.cell.2005.06.007.
4. Meng Z, Moroishi T, Mottier-Pavie V, Plouffe SW, Hansen CG, Hong AW, *et al.* MAP4K family kinases act in parallel to MST1/2 to activate LATS1/2 in the Hippo pathway. Nat Commun **2015**;6:8357 doi 10.1038/ncomms9357.
5. Zheng Y, Wang W, Liu B, Deng H, Uster E, Pan D. Identification of Happyhour/MAP4K as Alternative Hpo/Mst-like Kinases in the Hippo Kinase Cascade. Dev Cell **2015**;34(6):642-55 doi 10.1016/j.devcel.2015.08.014.
6. Li Q, Li S, Mana-Capelli S, Roth Flach RJ, Danai LV, Amcheslavsky A, *et al.* The conserved misshapen-warts-Yorkie pathway acts in enteroblasts to regulate intestinal stem cells in Drosophila. Dev Cell **2014**;31(3):291-304 doi 10.1016/j.devcel.2014.09.012.
7. Li S, Cho YS, Yue T, Ip YT, Jiang J. Overlapping functions of the MAP4K family kinases Hppy and Msn in Hippo signaling. Cell Discov **2015**;1:15038 doi 10.1038/celldisc.2015.38.
8. Zhang N, Bai H, David KK, Dong J, Zheng Y, Cai J, *et al.* The Merlin/NF2 tumor suppressor functions through the YAP oncoprotein to regulate tissue homeostasis in mammals. Dev Cell **2010**;19(1):27-38 doi 10.1016/j.devcel.2010.06.015.
9. Yin F, Yu J, Zheng Y, Chen Q, Zhang N, Pan D. Spatial organization of Hippo signaling at the plasma membrane mediated by the tumor suppressor Merlin/NF2. Cell **2013**;154(6):1342-55 doi 10.1016/j.cell.2013.08.025.
10. Merrill JR, Inguscio A, Chung T, Demestichas B, Garcia LA, Habel J, *et al.* Sensitive, non-immunogenic in vivo imaging of cancer metastases and immunotherapy response. Cell Stress **2023**;7(8):59-68 doi 10.15698/cst2023.08.288.
11. Zhao B, Ye X, Yu J, Li L, Li W, Li S, *et al.* TEAD mediates YAP-dependent gene induction and growth control. Genes Dev **2008**;22(14):1962-71 doi 10.1101/gad.1664408.
12. Goulev Y, Fauny JD, Gonzalez-Marti B, Flagiello D, Silber J, Zider A. SCALLOPED interacts with YORKIE, the nuclear effector of the hippo tumor-suppressor pathway in Drosophila. Curr Biol **2008**;18(6):435-41 doi 10.1016/j.cub.2008.02.034.
13. Zhang H, Liu CY, Zha ZY, Zhao B, Yao J, Zhao S, *et al.* TEAD transcription factors mediate the function of TAZ in cell growth and epithelial-mesenchymal transition. J Biol Chem **2009**;284(20):13355-62 doi 10.1074/jbc.M900843200.
14. Sanchez-Vega F, Mina M, Armenia J, Chatila WK, Luna A, La KC, *et al.* Oncogenic Signaling Pathways in The Cancer Genome Atlas. Cell **2018**;173(2):321-37 e10 doi 10.1016/j.cell.2018.03.035.
15. Zanconato F, Cordenonsi M, Piccolo S. YAP/TAZ at the Roots of Cancer. Cancer Cell **2016**;29(6):783-803 doi 10.1016/j.ccell.2016.05.005.
16. Chang L, Azzolin L, Di Biagio D, Zanconato F, Battilana G, Lucon Xiccato R, *et al.* The SWI/SNF complex is a mechanoregulated inhibitor of YAP and TAZ. Nature **2018**;563(7730):265-9 doi 10.1038/s41586-018-0658-1.
17. Mo JS, Meng Z, Kim YC, Park HW, Hansen CG, Kim S, *et al.* Cellular energy stress induces AMPK-mediated regulation of YAP and the Hippo pathway. Nat Cell Biol **2015**;17(4):500-10 doi 10.1038/ncb3111.

18. Yang CC, Graves HK, Moya IM, Tao C, Hamaratoglu F, Gladden AB, *et al.* Differential regulation of the Hippo pathway by adherens junctions and apical-basal cell polarity modules. Proc Natl Acad Sci U S A **2015**;112(6):1785-90 doi 10.1073/pnas.1420850112.
19. Dupont S, Morsut L, Aragona M, Enzo E, Giulitti S, Cordenonsi M, *et al.* Role of YAP/TAZ in mechanotransduction. Nature **2011**;474(7350):179-83 doi 10.1038/nature10137.
20. Meng Z, Qiu Y, Lin KC, Kumar A, Placone JK, Fang C, *et al.* RAP2 mediates mechanoresponses of the Hippo pathway. Nature **2018**;560(7720):655-60 doi 10.1038/s41586-018-0444-0.
21. Azzolin L, Panciera T, Soligo S, Enzo E, Bicciato S, Dupont S, *et al.* YAP/TAZ incorporation in the beta-catenin destruction complex orchestrates the Wnt response. Cell **2014**;158(1):157-70 doi 10.1016/j.cell.2014.06.013.
22. Kowalczyk W, Romanelli L, Atkins M, Hillen H, Bravo Gonzalez-Blas C, Jacobs J, *et al.* Hippo signaling instructs ectopic but not normal organ growth. Science **2022**;378(6621):eabg3679 doi 10.1126/science.abg3679.
23. Donato E, Biagioni F, Bisso A, Caganova M, Amati B, Campaner S. YAP and TAZ are dispensable for physiological and malignant haematopoiesis. Leukemia **2018**;32(9):2037-40 doi 10.1038/s41375-018-0111-3.
24. Pobbati AV, Han X, Hung AW, Weiguang S, Huda N, Chen GY, *et al.* Targeting the Central Pocket in Human Transcription Factor TEAD as a Potential Cancer Therapeutic Strategy. Structure **2015**;23(11):2076-86 doi 10.1016/j.str.2015.09.009.
25. Bum-Erdene K, Zhou D, Gonzalez-Gutierrez G, Ghozayel MK, Si Y, Xu D, *et al.* Small-Molecule Covalent Modification of Conserved Cysteine Leads to Allosteric Inhibition of the TEAD·Yap Protein-Protein Interaction. Cell Chem Biol **2019**;26(3):378-89 e13 doi 10.1016/j.chembiol.2018.11.010.
26. Furet P, Bordas V, Le Douget M, Salem B, Mesrouze Y, Imbach-Weese P, *et al.* The First Class of Small Molecules Potently Disrupting the YAP-TEAD Interaction by Direct Competition. ChemMedChem **2022**;17(19):e202200303 doi 10.1002/cmdc.202200303.
27. Hagenbeek TJ, Zbieg JR, Hafner M, Mroue R, Lacap JA, Sodir NM, *et al.* An allosteric pan-TEAD inhibitor blocks oncogenic YAP/TAZ signaling and overcomes KRAS G12C inhibitor resistance. Nat Cancer **2023**;4(6):812-28 doi 10.1038/s43018-023-00577-0.
28. Kemphues KJ, Priess JR, Morton DG, Cheng NS. Identification of genes required for cytoplasmic localization in early C. elegans embryos. Cell **1988**;52(3):311-20 doi 10.1016/s0092-8674(88)80024-2.
29. Drewes G, Ebneth A, Preuss U, Mandelkow EM, Mandelkow E. MARK, a novel family of protein kinases that phosphorylate microtubule-associated proteins and trigger microtubule disruption. Cell **1997**;89(2):297-308 doi 10.1016/s0092-8674(00)80208-1.
30. Hurov JB, Watkins JL, Piwnica-Worms H. Atypical PKC phosphorylates PAR-1 kinases to regulate localization and activity. Curr Biol **2004**;14(8):736-41 doi 10.1016/j.cub.2004.04.007.
31. Biernat J, Wu YZ, Timm T, Zheng-Fischhofer Q, Mandelkow E, Meijer L, *et al.* Protein kinase MARK/PAR-1 is required for neurite outgrowth and establishment of neuronal polarity. Mol Biol Cell **2002**;13(11):4013-28 doi 10.1091/mbc.02-03-0046.
32. Lizcano JM, Goransson O, Toth R, Deak M, Morrice NA, Boudeau J, *et al.* LKB1 is a master kinase that activates 13 kinases of the AMPK subfamily, including MARK/PAR-1. EMBO J **2004**;23(4):833-43 doi 10.1038/sj.emboj.7600110.
33. Huang HL, Wang S, Yin MX, Dong L, Wang C, Wu W, *et al.* Par-1 regulates tissue growth by influencing hippo phosphorylation status and hippo-salvador association. PLoS Biol **2013**;11(8):e1001620 doi 10.1371/journal.pbio.1001620.

34. Spilker AC, Rabilotta A, Zbinden C, Labbe JC, Gotta M. MAP kinase signaling antagonizes PAR-1 function during polarization of the early Caenorhabditis elegans embryo. Genetics **2009**;183(3):965-77 doi 10.1534/genetics.109.106716.
35. Shi J, Wang E, Milazzo JP, Wang Z, Kinney JB, Vakoc CR. Discovery of cancer drug targets by CRISPR-Cas9 screening of protein domains. Nat Biotechnol **2015**;33(6):661-7 doi 10.1038/nbt.3235.
36. Han K, Jeng EE, Hess GT, Morgens DW, Li A, Bassik MC. Synergistic drug combinations for cancer identified in a CRISPR screen for pairwise genetic interactions. Nat Biotechnol **2017**;35(5):463-74 doi 10.1038/nbt.3834.
37. Zhao D, Badur MG, Luebeck J, Magana JH, Birmingham A, Sasik R, *et al.* Combinatorial CRISPR-Cas9 Metabolic Screens Reveal Critical Redox Control Points Dependent on the KEAP1-NRF2 Regulatory Axis. Mol Cell **2018**;69(4):699-708 e7 doi 10.1016/j.molcel.2018.01.017.
38. Shen JP, Zhao D, Sasik R, Luebeck J, Birmingham A, Bojorquez-Gomez A, *et al.* Combinatorial CRISPR-Cas9 screens for de novo mapping of genetic interactions. Nat Methods **2017**;14(6):573-6 doi 10.1038/nmeth.4225.
39. Thompson NA, Ranzani M, van der Weyden L, Iyer V, Offord V, Droop A, *et al.* Combinatorial CRISPR screen identifies fitness effects of gene paralogues. Nat Commun **2021**;12(1):1302 doi 10.1038/s41467-021-21478-9.
40. Parrish PCR, Thomas JD, Gabel AM, Kamlapurkar S, Bradley RK, Berger AH. Discovery of synthetic lethal and tumor suppressor paralog pairs in the human genome. Cell Rep **2021**;36(9):109597 doi 10.1016/j.celrep.2021.109597.
41. Najm FJ, Strand C, Donovan KF, Hegde M, Sanson KR, Vaimberg EW, *et al.* Orthologous CRISPR-Cas9 enzymes for combinatorial genetic screens. Nat Biotechnol **2018**;36(2):179-89 doi 10.1038/nbt.4048.
42. Ito T, Young MJ, Li R, Jain S, Wernitznig A, Krill-Burger JM, *et al.* Paralog knockout profiling identifies DUSP4 and DUSP6 as a digenic dependence in MAPK pathway-driven cancers. Nat Genet **2021**;53(12):1664-72 doi 10.1038/s41588-021-00967-z.
43. Zamanighomi M, Jain SS, Ito T, Pal D, Daley TP, Sellers WR. GEMINI: a variational Bayesian approach to identify genetic interactions from combinatorial CRISPR screens. Genome Biol **2019**;20(1):137 doi 10.1186/s13059-019-1745-9.
44. Wilting RH, Yanover E, Heideman MR, Jacobs H, Horner J, van der Torre J, *et al.* Overlapping functions of Hdac1 and Hdac2 in cell cycle regulation and haematopoiesis. EMBO J **2010**;29(15):2586-97 doi 10.1038/emboj.2010.136.
45. Welti J, Sharp A, Brooks N, Yuan W, McNair C, Chand SN, *et al.* Targeting the p300/CBP Axis in Lethal Prostate Cancer. Cancer Discov **2021**;11(5):1118-37 doi 10.1158/2159-8290.CD-20-0751.
46. Kawasumi R, Abe T, Arakawa H, Garre M, Hirota K, Branzei D. ESCO1/2's roles in chromosome structure and interphase chromatin organization. Genes Dev **2017**;31(21):2136-50 doi 10.1101/gad.306084.117.
47. Zeng Y, Yin L, Zhou J, Zeng R, Xiao Y, Black AR, *et al.* MARK2 regulates chemotherapeutic responses through class IIa HDAC-YAP axis in pancreatic cancer. Oncogene **2022**;41(31):3859-75 doi 10.1038/s41388-022-02399-3.
48. Machino H, Kaneko S, Komatsu M, Ikawa N, Asada K, Nakato R, *et al.* The metabolic stress-activated checkpoint LKB1-MARK3 axis acts as a tumor suppressor in high-grade serous ovarian carcinoma. Commun Biol **2022**;5(1):39 doi 10.1038/s42003-021-02992-4.
49. Ooki T, Murata-Kamiya N, Takahashi-Kanemitsu A, Wu W, Hatakeyama M. High-Molecular-Weight Hyaluronan Is a Hippo Pathway Ligand Directing Cell Density-Dependent Growth Inhibition via PAR1b. Dev Cell **2019**;49(4):590-604 e9 doi 10.1016/j.devcel.2019.04.018.

50. Islam K. The Bump-and-Hole Tactic: Expanding the Scope of Chemical Genetics. Cell Chem Biol **2018**;25(10):1171-84 doi 10.1016/j.chembiol.2018.07.001.
51. Wang Y, Xu X, Maglic D, Dill MT, Mojumdar K, Ng PK, *et al.* Comprehensive Molecular Characterization of the Hippo Signaling Pathway in Cancer. Cell Rep **2018**;25(5):1304-17 e5 doi 10.1016/j.celrep.2018.10.001.
52. Rausch V, Bostrom JR, Park J, Bravo IR, Feng Y, Hay DC, *et al.* The Hippo Pathway Regulates Caveolae Expression and Mediates Flow Response via Caveolae. Curr Biol **2019**;29(2):242-55 e6 doi 10.1016/j.cub.2018.11.066.
53. Seo E, Basu-Roy U, Gunaratne PH, Coarfa C, Lim DS, Basilico C, *et al.* SOX2 regulates YAP1 to maintain stemness and determine cell fate in the osteo-adipo lineage. Cell Rep **2013**;3(6):2075-87 doi 10.1016/j.celrep.2013.05.029.
54. Heidary Arash E, Shiban A, Song S, Attisano L. MARK4 inhibits Hippo signaling to promote proliferation and migration of breast cancer cells. EMBO Rep **2017**;18(3):420-36 doi 10.15252/embr.201642455.
55. Hertz NT, Wang BT, Allen JJ, Zhang C, Dar AC, Burlingame AL, *et al.* Chemical genetic approach for kinase-substrate mapping by covalent capture of thiophosphopeptides and analysis by mass spectrometry. Curr Protoc Chem Biol **2010**;2(1):15-36 doi 10.1002/9780470559277.ch090201.
56. Ogg S, Gabrielli B, Piwnica-Worms H. Purification of a serine kinase that associates with and phosphorylates human Cdc25C on serine 216. J Biol Chem **1994**;269(48):30461-9.
57. Tang X, Jang SW, Wang X, Liu Z, Bahr SM, Sun SY, *et al.* Akt phosphorylation regulates the tumour-suppressor merlin through ubiquitination and degradation. Nat Cell Biol **2007**;9(10):1199-207 doi 10.1038/ncb1641.
58. Yu FX, Zhao B, Panupinthu N, Jewell JL, Lian I, Wang LH, *et al.* Regulation of the Hippo-YAP pathway by G-protein-coupled receptor signaling. Cell **2012**;150(4):780-91 doi 10.1016/j.cell.2012.06.037.
59. Kanai F, Marignani PA, Sarbassova D, Yagi R, Hall RA, Donowitz M, *et al.* TAZ: a novel transcriptional co-activator regulated by interactions with 14-3-3 and PDZ domain proteins. EMBO J **2000**;19(24):6778-91 doi 10.1093/emboj/19.24.6778.
60. Hong AW, Meng Z, Yuan HX, Plouffe SW, Moon S, Kim W, *et al.* Osmotic stress-induced phosphorylation by NLK at Ser128 activates YAP. EMBO Rep **2017**;18(1):72-86 doi 10.15252/embr.201642681.
61. Moon S, Kim W, Kim S, Kim Y, Song Y, Bilousov O, *et al.* Phosphorylation by NLK inhibits YAP-14-3-3-interactions and induces its nuclear localization. EMBO Rep **2017**;18(1):61-71 doi 10.15252/embr.201642683.
62. Saadat I, Higashi H, Obuse C, Umeda M, Murata-Kamiya N, Saito Y, *et al.* Helicobacter pylori CagA targets PAR1/MARK kinase to disrupt epithelial cell polarity. Nature **2007**;447(7142):330-3 doi 10.1038/nature05765.
63. Nesic D, Miller MC, Quinkert ZT, Stein M, Chait BT, Stebbins CE. Helicobacter pylori CagA inhibits PAR1-MARK family kinases by mimicking host substrates. Nat Struct Mol Biol **2010**;17(1):130-2 doi 10.1038/nsmb.1705.
64. Pearson JD, Huang K, Pacal M, McCurdy SR, Lu S, Aubry A, *et al.* Binary pan-cancer classes with distinct vulnerabilities defined by pro- or anti-cancer YAP/TEAD activity. Cancer Cell **2021**;39(8):1115-34 e12 doi 10.1016/j.ccell.2021.06.016.
65. Shue YT, Drainas AP, Li NY, Pearsall SM, Morgan D, Sinnott-Armstrong N, *et al.* A conserved YAP/Notch/REST network controls the neuroendocrine cell fate in the lungs. Nat Commun **2022**;13(1):2690 doi 10.1038/s41467-022-30416-2.

66. Cottini F, Hideshima T, Xu C, Sattler M, Dori M, Agnelli L, *et al.* Rescue of Hippo coactivator YAP1 triggers DNA damage-induced apoptosis in hematological cancers. Nat Med **2014**;20(6):599-606 doi 10.1038/nm.3562.
67. Piccolo S, Panciera T, Contessotto P, Cordenonsi M. YAP/TAZ as master regulators in cancer: modulation, function and therapeutic approaches. Nat Cancer **2023**;4(1):9-26 doi 10.1038/s43018-022-00473-z.
68. Battilana G, Zanconato F, Piccolo S. Mechanisms of YAP/TAZ transcriptional control. Cell Stress **2021**;5(11):167-72 doi 10.15698/cst2021.11.258.
69. Shulman JM, Benton R, St Johnston D. The Drosophila homolog of C. elegans PAR-1 organizes the oocyte cytoskeleton and directs oskar mRNA localization to the posterior pole. Cell **2000**;101(4):377-88 doi 10.1016/s0092-8674(00)80848-x.
70. Mohseni M, Sun J, Lau A, Curtis S, Goldsmith J, Fox VL, *et al.* A genetic screen identifies an LKB1-MARK signalling axis controlling the Hippo-YAP pathway. Nat Cell Biol **2014**;16(1):108-17 doi 10.1038/ncb2884.
71. Kaneda A, Seike T, Danjo T, Nakajima T, Otsubo N, Yamaguchi D, *et al.* The novel potent TEAD inhibitor, K-975, inhibits YAP1/TAZ-TEAD protein-protein interactions and exerts an anti-tumor effect on malignant pleural mesothelioma. Am J Cancer Res **2020**;10(12):4399-415.
72. Dey A, Varelas X, Guan KL. Targeting the Hippo pathway in cancer, fibrosis, wound healing and regenerative medicine. Nat Rev Drug Discov **2020**;19(7):480-94 doi 10.1038/s41573-020-0070-z.
73. Cohen P, Cross D, Janne PA. Kinase drug discovery 20 years after imatinib: progress and future directions. Nat Rev Drug Discov **2021**;20(7):551-69 doi 10.1038/s41573-021-00195-4.
74. Lu H, Zhou Q, He J, Jiang Z, Peng C, Tong R, *et al.* Recent advances in the development of protein-protein interactions modulators: mechanisms and clinical trials. Signal Transduct Target Ther **2020**;5(1):213 doi 10.1038/s41392-020-00315-3.
75. Olah J, Szenasi T, Lehotzky A, Norris V, Ovadi J. Challenges in Discovering Drugs That Target the Protein-Protein Interactions of Disordered Proteins. Int J Mol Sci **2022**;23(3) doi 10.3390/ijms23031550.
76. Sun Y, Hu L, Tao Z, Jarugumilli GK, Erb H, Singh A, *et al.* Pharmacological blockade of TEAD-YAP reveals its therapeutic limitation in cancer cells. Nat Commun **2022**;13(1):6744 doi 10.1038/s41467-022-34559-0.
77. Kapoor A, Yao W, Ying H, Hua S, Liewen A, Wang Q, *et al.* Yap1 activation enables bypass of oncogenic Kras addiction in pancreatic cancer. Cell **2014**;158(1):185-97 doi 10.1016/j.cell.2014.06.003.
78. Mukhopadhyay S, Huang HY, Lin Z, Ranieri M, Li S, Sahu S, *et al.* Genome-Wide CRISPR Screens Identify Multiple Synthetic Lethal Targets That Enhance KRASG12C Inhibitor Efficacy. Cancer Res **2023**;83(24):4095-111 doi 10.1158/0008-5472.CAN-23-2729.
79. Edwards AC, Stalnecker CA, Jean Morales A, Taylor KE, Klomp JE, Klomp JA, *et al.* TEAD Inhibition Overcomes YAP1/TAZ-Driven Primary and Acquired Resistance to KRASG12C Inhibitors. Cancer Res **2023**;83(24):4112-29 doi 10.1158/0008-5472.CAN-23-2994.
80. Baroja I, Kyriakidis NC, Halder G, Moya IM. Expected and unexpected effects after systemic inhibition of Hippo transcriptional output in cancer. Nat Commun **2024**;15(1):2700 doi 10.1038/s41467-024-46531-1.
81. Shao DD, Xue W, Krall EB, Bhutkar A, Piccioni F, Wang X, *et al.* KRAS and YAP1 converge to regulate EMT and tumor survival. Cell **2014**;158(1):171-84 doi 10.1016/j.cell.2014.06.004.
82. Wasko UN, Jiang J, Dalton TC, Curiel-Garcia A, Edwards AC, Wang Y, *et al.* Tumour-selective activity of RAS-GTP inhibition in pancreatic cancer. Nature **2024**;629(8013):927-36 doi 10.1038/s41586-024-07379-z.

83. Tiriac H, Belleau P, Engle DD, Plenker D, Deschenes A, Somerville TDD, *et al.* Organoid Profiling Identifies Common Responders to Chemotherapy in Pancreatic Cancer. Cancer Discov **2018**;8(9):1112-29 doi 10.1158/2159-8290.CD-18-0349.
84. Bhatia S, Kramer M, Russo S, Naik P, Arun G, Brophy K, *et al.* Patient-Derived Triple-Negative Breast Cancer Organoids Provide Robust Model Systems That Recapitulate Tumor Intrinsic Characteristics. Cancer Res **2022**;82(7):1174-92 doi 10.1158/0008-5472.CAN-21-2807.
85. Li R, Klingbeil O, Monducci D, Young MJ, Rodriguez DJ, Bayyat Z, *et al.* Comparative optimization of combinatorial CRISPR screens. Nat Commun **2022**;13(1):2469 doi 10.1038/s41467-022-30196-9.
86. Marchler-Bauer A, Derbyshire MK, Gonzales NR, Lu S, Chitsaz F, Geer LY, *et al.* CDD: NCBI's conserved domain database. Nucleic Acids Res **2015**;43(Database issue):D222-6 doi 10.1093/nar/gku1221.
87. Barretina J, Caponigro G, Stransky N, Venkatesan K, Margolin AA, Kim S, *et al.* The Cancer Cell Line Encyclopedia enables predictive modelling of anticancer drug sensitivity. Nature **2012**;483(7391):603-7 doi 10.1038/nature11003.
88. Tate JG, Bamford S, Jubb HC, Sondka Z, Beare DM, Bindal N, *et al.* COSMIC: the Catalogue Of Somatic Mutations In Cancer. Nucleic Acids Res **2019**;47(D1):D941-D7 doi 10.1093/nar/gky1015.
89. Consortium GT. The Genotype-Tissue Expression (GTEx) project. Nat Genet **2013**;45(6):580-5 doi 10.1038/ng.2653.
90. Bray NL, Pimentel H, Melsted P, Pachter L. Near-optimal probabilistic RNA-seq quantification. Nat Biotechnol **2016**;34(5):525-7 doi 10.1038/nbt.3519.
91. Langmead B, Salzberg SL. Fast gapped-read alignment with Bowtie 2. Nat Methods **2012**;9(4):357-9 doi 10.1038/nmeth.1923.
92. Feng J, Liu T, Qin B, Zhang Y, Liu XS. Identifying ChIP-seq enrichment using MACS. Nat Protoc **2012**;7(9):1728-40 doi 10.1038/nprot.2012.101.
93. Subramanian A, Tamayo P, Mootha VK, Mukherjee S, Ebert BL, Gillette MA, *et al.* Gene set enrichment analysis: a knowledge-based approach for interpreting genome-wide expression profiles. Proc Natl Acad Sci U S A **2005**;102(43):15545-50 doi 10.1073/pnas.0506580102.
94. Klingbeil O, Lesche R, Gelato KA, Haendler B, Lejeune P. Inhibition of BET bromodomain-dependent XIAP and FLIP expression sensitizes KRAS-mutated NSCLC to pro-apoptotic agents. Cell Death Dis **2016**;7(9):e2365 doi 10.1038/cddis.2016.271.

Fig. 1. Paralog co-targeting CRISPR screens identify MARK2/3 as context-specific cancer dependencies. A, **B**, Workflow of paralog double knockout CRISPR screens including paralog identification, domain mapping, sgRNA design, oligo synthesis, cloning, and negative selection screening. Numbers of paralog combinations are indicated. **B,** CRISPR screening results summary, analysis of synergy between paralog gene pairs (GEMINI score) (**Supplementary Table 4-6**) maximum scores are shown together with variance of dependency (variance of average $\log_2$(fold-change) of double guide RNA abundance) across 22 cell lines screened. Each dot represents a double knockout paralog-pair (n=2,726) among signaling- and epigenetic regulators. **C**, **D,** Competition-based fitness assays in Cas9-expressing cancer cells after lentiviral knockout of indicated genes (expression of double guide RNAs (dgRNA) was linked to GFP). c, Heatmap color indicates the $\log_2$(fold-change) of normalized GFP (%GFP$^+$ normalized to day 3 or 6 after infection). n=3. d, Competition-based fitness assays in the indicated cell lines. Data are shown as mean ± SD of normalized %GFP$^+$ (to day 3 after infection). n=3. **E**, Western blot analysis of the indicated cell lines. **F**, Apoptosis measurements using Annexin-V and DAPI in Cas9-expressing YAPC cells. Indicated genes were knocked out using lentiviral dgRNAs linked to GFP. Data are shown as mean ± SD. n=3-6. *P* value was calculated on change in viability compared to control with one-way ANOVA and Dunnett's correction. **G**, Crystal violet stain of indicated cells following lentiviral knockout of indicated genes. Data shown are representative of three independent biological replicates. **H**, Rescue experiment in YAPC cells using lentiviral expression of CRISPR resistant (CR) cDNAs or empty vector control (Ctrl). Data shown are the mean ± SD of %GFP$^+$ (normalized to day 3 after infection). n=3. *P* values are calculated using a mixed effects model (considering the interaction of experimental groups over time) compared to Ctrl group and corrected with Bonferroni-Holm (BH). **I**, Normalized relative luminescence units (RLU) from CellTiter-Glo viability measurements of the indicated YAPC cell lines following 5 days of 1NM-PP1 treatment. Data are shown as mean ± SD. n=9 measurements from three biological replicates performed in triplicate. Four-parameter dose-response curves were plotted.

Fig. 2. MARK2/3 dependency in cancer is linked to the maintenance of YAP/TAZ function. **A**, mRNA expression differences comparing 19 MARK2/3-dependent to 12 MARK2/3-independent human cancer cell lines. Transcriptome data were obtained from the CCLE database, KLM-1 (GSE140484) and CHL-1 (this paper). TPM, transcripts per million were calculated and the difference in $\log_2$(TPM+1) was plotted. *P* values were calculated using Empirical Bayes Statistics (eBayes) for differential expression with BH correction. **B**, Heatmap of MARK2/3 dependent and independent cancer cell lines showing dependence on YAP/TAZ and expression of target genes. Competition-based fitness assays in Cas9-expressing cancer cells after lentiviral knockout of indicated genes (expression of dgRNAs was linked with GFP). Heatmap color indicates the $\log_2$(fold-change) of %GFP$^+$ (normalized to day 3 or 6 after infection). n=3. **C**, Crystal violet stain of indicated cells following lentiviral knockout of indicated genes. Data shown are representative of three independent biological replicates. **D**, Flow cytometry histogram of YAP/TAZ:TEAD reporter assay (19) in MDA-MB231 cells, on day 9 post-infection. Data are representative of three independent experiments. **E,** Gene set enrichment analysis (GSEA) of Cas9$^+$ MDA-MB231 cancer cells following MARK2+3^{dKO}, including normalized enrichment score (NES) and *P* value. **F,** Heatmap showing the GSEA NES for the YAP/TAZ gene signature following MARK2+3^{dKO} in dependent and independent cell lines. **G,** Heatmap of mRNA expression ($\log_2$(normalized count)) z-scores in Cas9$^+$ MDA-MB231 cells of genes significantly down- or up regulated upon MARK2+3^{dKO}. Expression values of down genes (n=188) and up genes (n=91) of two replicate samples following gene knockout were grouped based on unsupervised clustering. Significant differentially expressed genes were defined as adjusted *P* value $<10^{-4}$ and $\log_2$(fold-change) >2 or <-1. *P* values from Wald test (DEseq2) adjusted using BH. **H,** CUT&RUN density profile of YAP:TEAD4 bound, YAP/TAZ^{dKO} sensitive H3K27ac marked enhancer loci (n=7,896) following MARK2+3^{dKO}. Profiles shown are an average of 50bp bins around the summit of the enhancers. **I,** Occupancy profiles of public Chromatin immunoprecipitation sequencing (ChIP-seq) (TEAD4, YAP) (GSE66083) and CUT&RUN (H3K27ac) upon indicated gene knockout at YAP/TAZ target gene loci.

Fig. 3. MARK2/3 suppress the Hippo pathway and phosphorylate multiple components. **A**, Illustration of the Hippo pathway. **B**, **C,** Western blot analysis of Cas9$^+$ YAPC cells b, whole cell lysate or c, following fractionation into nuclear (Nuc) and cytosolic (Cyto) fraction, following control^{dKO} (Ctrl) or MARK2+3^{dKO}. Independent double guide RNAs (dgRNA) are indicated. **D**, Illustration of in-cell phosphorylation assay. Epitope-tagged cDNAs coding for putative MARK2-substrates are transfected into HEK-293T cells together with cDNA coding for analog-sensitive mutant MARK2^{M129G}. Kinase assay is performed using ATP analog (6-Fu-ATP-γ-S) selective for MARK2^{M129G}. Labeled substrates are alkylated using p-nitrobenzyl mesylate (PNBM) and identified following purification by western blot analysis. **E**, Western blot analysis of MARK2 specific in-cell phosphorylation of Hippo pathway components. Data are representative of two independent experiments. **F-H,** Lolli-pop illustration of MARK2-dependent phosphorylation sites on NF2, YAP and TAZ identified using mass spectrometry-based phosphoproteomics. C-term=carboxy-terminal domain, TB=TEAD binding domain, TAD=transactivation domain. A,D,F-H were created with BioRender.com

Fig. 4. MARK2/3 catalyze inhibitory phosphorylation of NF2 and activating phosphorylation of YAP/TAZ.

A, IP–western blot analysis evaluating the phosphorylation p-LATS1 (T1079) in the presence or absence of MARK2 or MARK3 following NF2 overexpression in HEK-293T cells. Data are representative of two independent experiments. **B**, IP–western blot analysis evaluating the phosphorylation p-LATS1 (T1079) after NF2 mutant overexpression in HEK-293T cells. Data are representative of two independent experiments. **C-E,** *In vitro* phosphorylation assay and IP–western blot analysis, evaluating the interaction of 14-3-3ε and recombinant LATS1 (rLATS1) or LATS2 (rLATS2) phosphorylated GST-YAP or GST-TAZ, following phosphorylation with recombinant MARK2 (rMARK2) or MARK3 (rMARK3). Data are representative of two independent experiments. **F**, IP–western blot analysis evaluating the interaction between 14-3-3ε and YAP^{5D} (phosphomimetic mutant), YAP^{5A} (phospho-null mutant) and controls YAP^{WT} (wild type) and YAP^{S127A} (LATS1/2 phosphosite/ 14-3-3 interaction mutant) in HEK-293T cells. Data are representative of two independent experiments. **G**, IP–western blot analysis evaluating the interaction between 14-3-3ε and TAZ^{4D} (phosphomimetic mutant), TAZ^{4A} (phospho-null mutant) and controls TAZ^{WT} (wild type) and TAZ^{S89A} (LATS1/2 phosphosite/ 14-3-3 interaction mutant) in HEK-293T cells. Data are representative of two independent experiments.

Fig. 5. Regulation of NF2 and YAP accounts for the essential functions of MARK2/3 in human cancer. A, Rescue experiment of MARK2+3^{dKO} following double knockout of *LATS1/2* or *MST1/2* and control double knockout Ctrl in indicated Cas9^{+} cell lines. Data shown are the mean ± SD of %GFP^{+} (normalized to day 3 after infection). n=3-6. *P* values are calculated using a mixed effects model (considering the interaction of experimental groups over time) compared to Ctrl group and corrected with Bonferroni-Holm (BH). **B**, **C,** Western blot analysis in YAPC cells and independent dgRNAs are indicated. **D**, Western blot analysis in Cas9^{+} YAPC cells. **E**, Rescue experiment of MARK2+3^{dKO} following knockout of *NF2* or Ctrl and lentiviral HA-YAP^{5D} overexpression. Data shown are the mean ± SD of %GFP^{+} (normalized to day 3 after infection). n=3. *P* values are calculated using a mixed effects model (considering the interaction of experimental groups over time) compared to Ctrl group and corrected with Bonferroni-Holm (BH).

Fig. 6. Inducible expression of a protein-based MARK2/3 inhibitor re-instates Hippo-mediated tumor suppression in organoid and xenograft tumor models. A, Illustration of MKI protein derived from *Helicobacter pylori* (*H.pylori*). Positioning of self-cleaving peptides (2A), GFP reporter, and number of amino acids are indicated. **B**, Competition-based fitness assays in YAPC cells after lentiviral expression of MKI^{WT} or MKI^{MUT}. **C**, Comparison of log_2(fold-change) of MKI and *MARK2+3*^{dKO} double knockout competition data in $Cas9^+$ cancer cell lines. Pearson correlation coefficient was calculated. Data shown are the mean of $\%GFP^+$ (normalized to day 3 after infection). n=3. **D**, global mRNA expression log_2(fold-change) correlation of MKI^{WT} vs MKI^{MUT} or MARK2+3^{dKO} vs $Ctrl^{KO}$ MDA-MB231 cells. **E**, Western blot analysis in YAPC cells 24h following doxycycline induced expression of indicated proteins. **F**, Rescue experiment of MKI^{WT} expression following knockout of *LATS1/2*, *NF2* or Ctrl and lentiviral HA-YAP^{5D} overexpression. Data shown are the mean ± SD of $\%GFP^+$ (normalized to day 3 after infection). n=3. *P* values are calculated using a mixed effects model (considering the interaction of experimental groups over time) compared to Ctrl group and corrected with Bonferroni-Holm (BH). **G**, Normalized relative luminescence units (RLU) from CellTiter-Glo viability measurements of the indicated human patient-derived triple-negative breast cancer (TNBC) or pancreatic ductal adenocarcinoma (PDAC) organoids following doxycycline (Dox) induced expression of MKI^{WT} for 10 days. Data shown are mean ± SEM. n=6 measurements from two biological replicates performed in triplicate. *P* value was calculated using a two-tailed parametric t-test with Welch's correction. **H**, Experimental design of orthotopic transplantation study. Mice were treated with doxycycline 17 days post-implantation and tumor growth was monitored using NIS-SPECT and bioluminescence imaging once every 7 days. **I**, Western blot analysis in T3M-4 cells 24h following doxycycline induced expression of MKI^{WT}. **J**, Representative microscopic images (n=2-3) showing immunohistochemistry of GFP following 24h treatment with doxycycline. scale bar 200µm. **K**, Growth kinetics of orthotopic PDAC T3M-4 xenografts implanted in immunodeficient mice. Expression of MKI^{WT} from doxycycline (Dox)-inducible lentiviral construct was induced on day 17 post-injection of the cells. Data are shown as mean ± SEM. n=10 per group. **L**, Representative bioluminescence measurement at indicated time points. A and H were created with BioRender.com

FIGURE 1

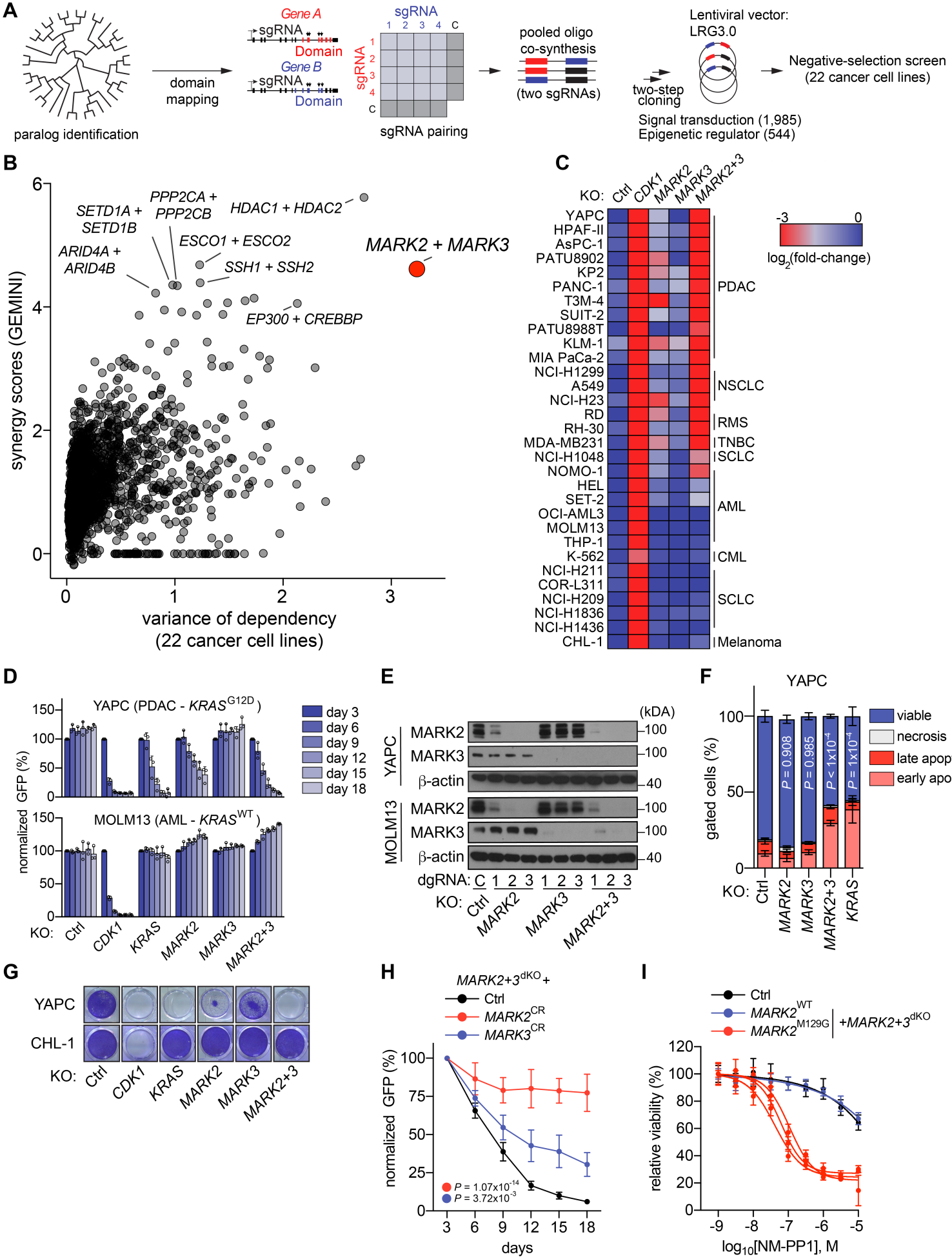

FIGURE 2

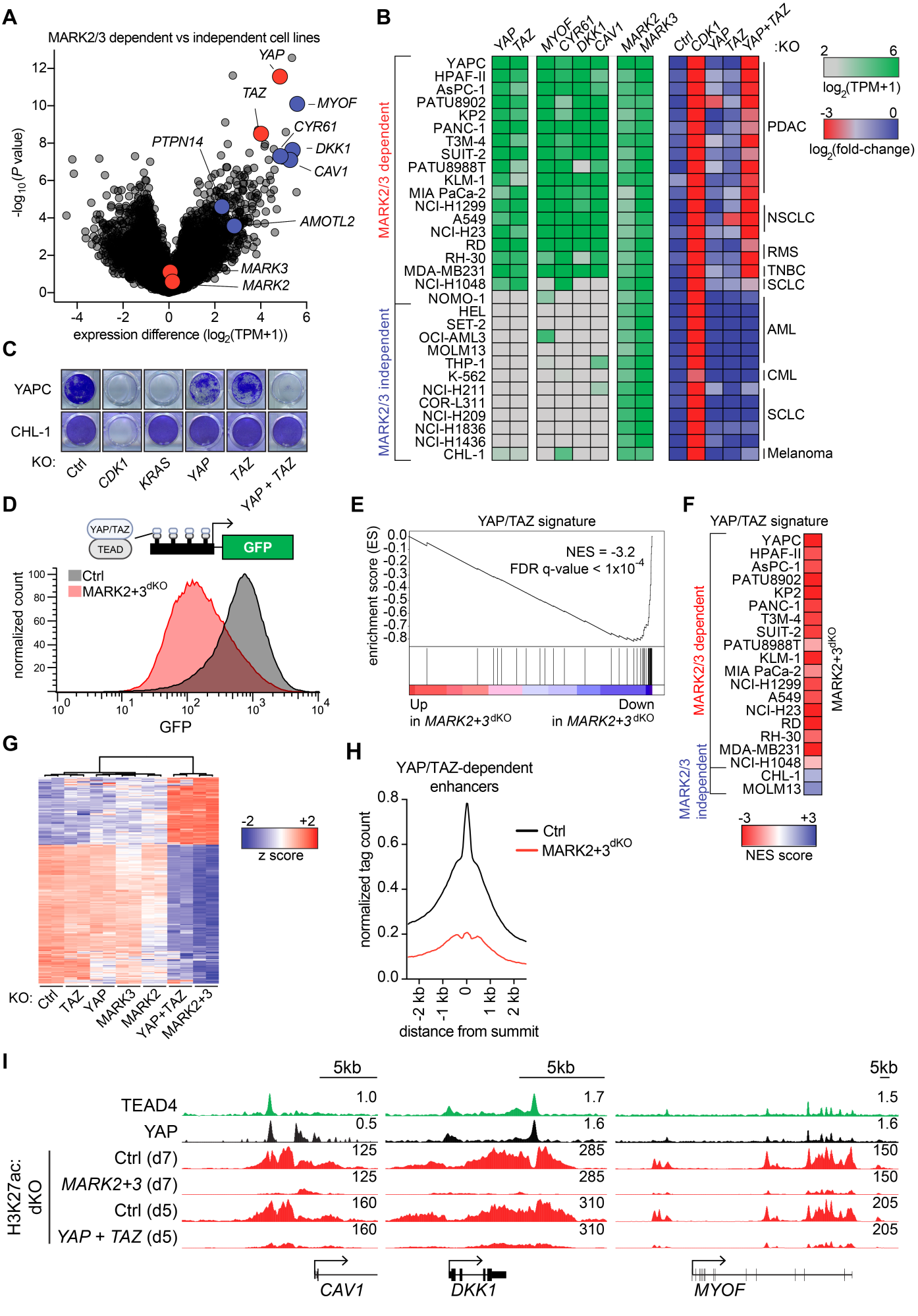

FIGURE 3

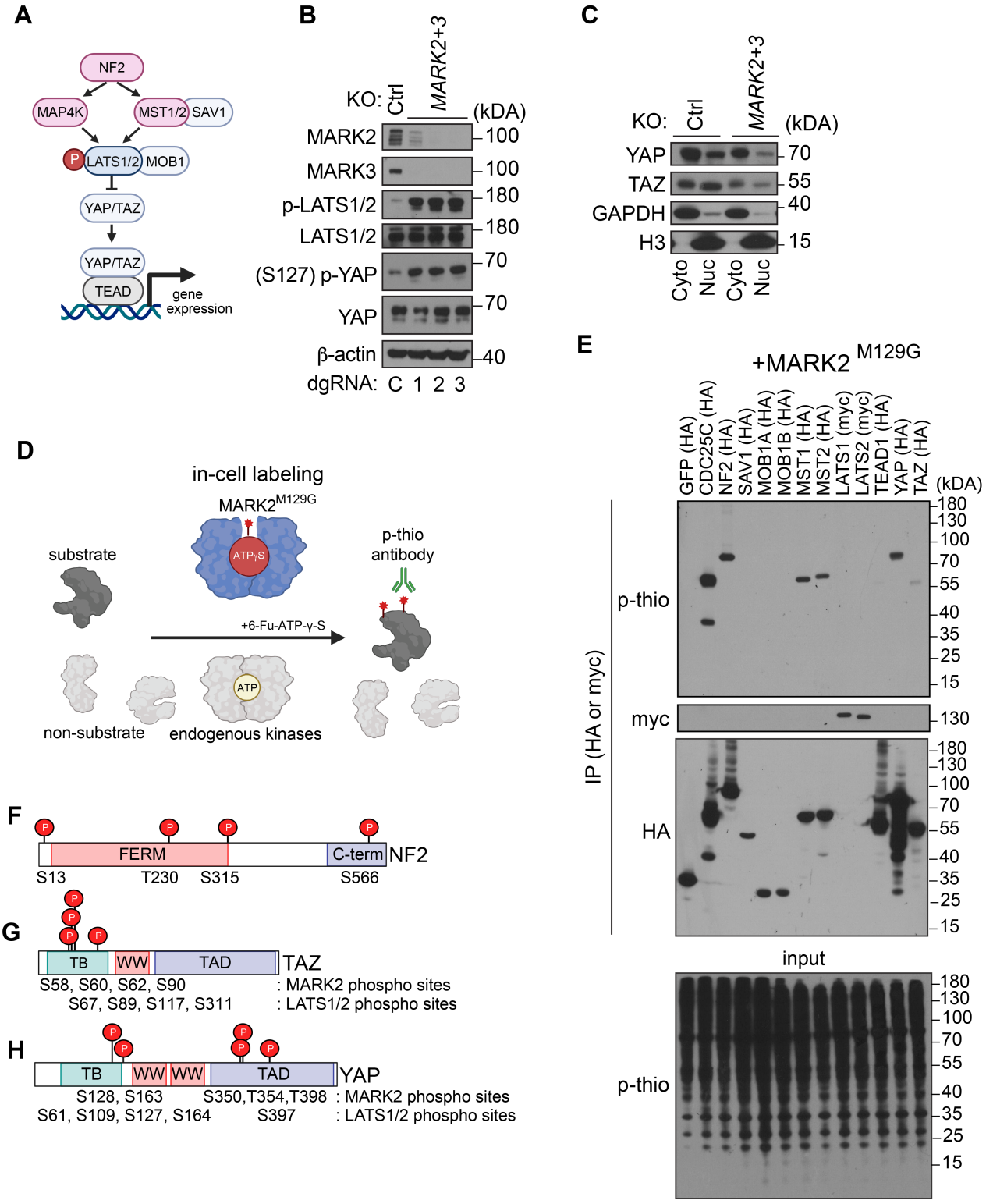

FIGURE 4

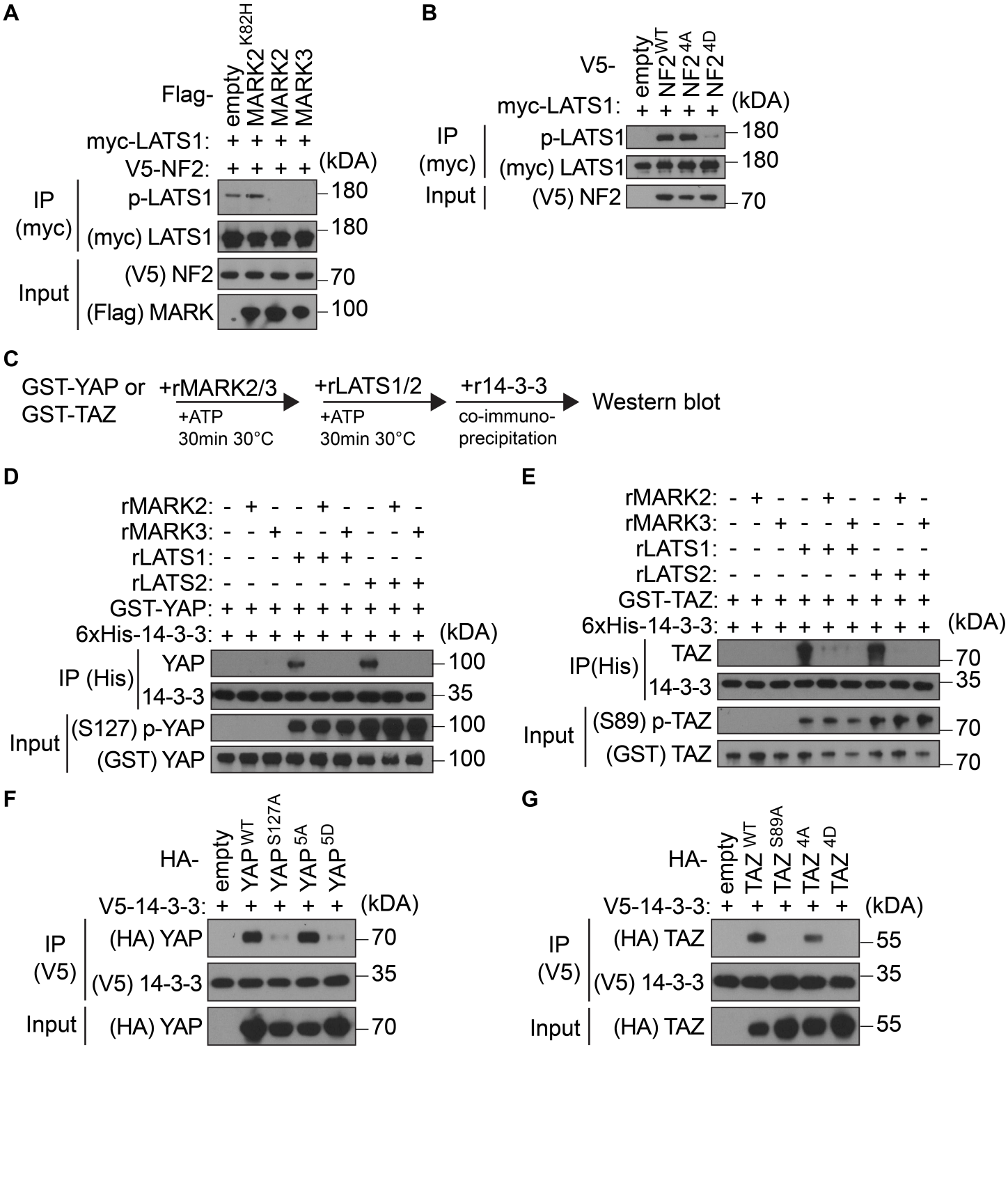

FIGURE 5

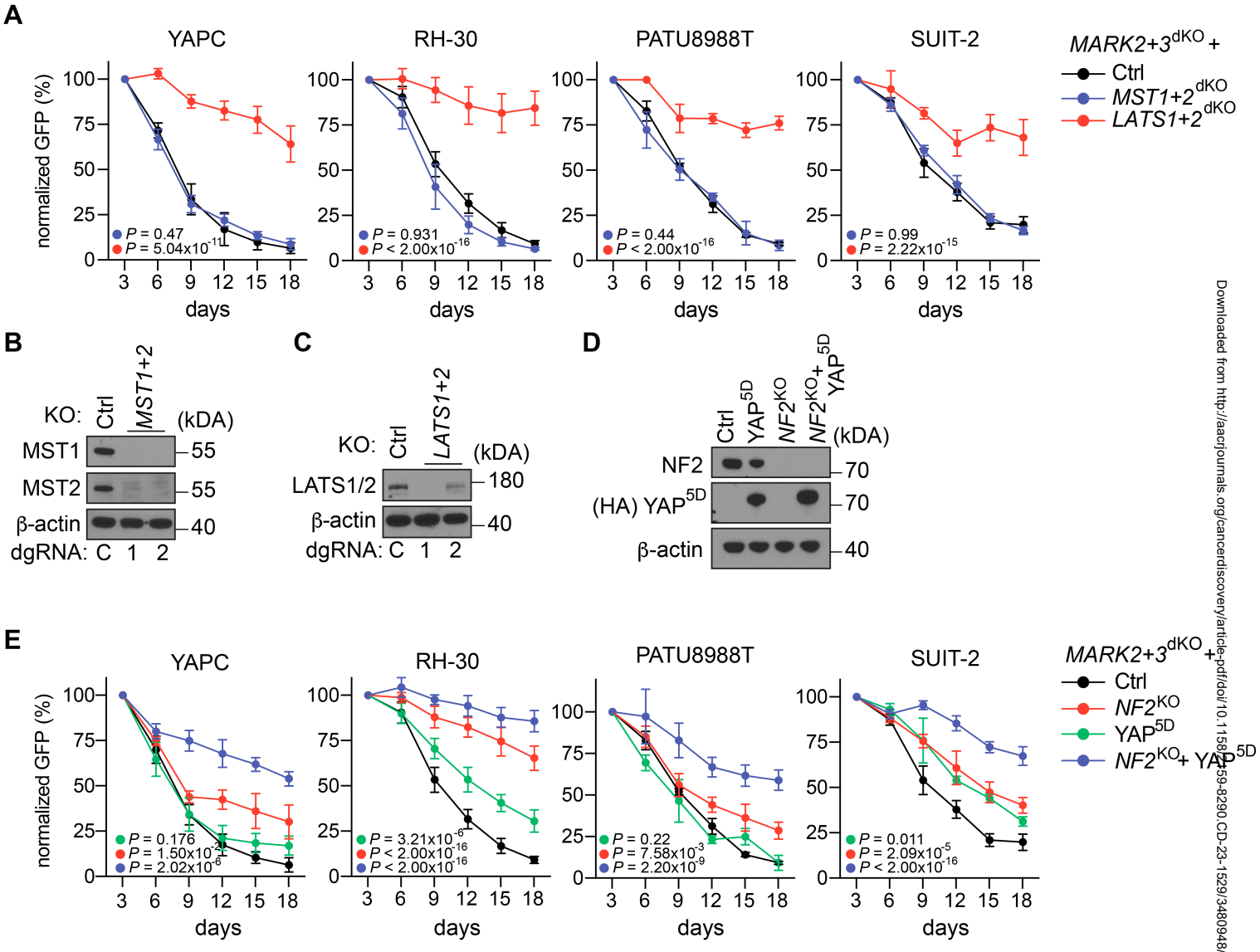

FIGURE 6